*Journal of Neurochemistry*, 2005, **94**, 1254–1263 doi:10.1111/j.1471-4159.2005.03272.x

# *In vivo* evidence of CHIP up-regulation attenuating tau aggregation

Naruhiko Sahara,* Miyuki Murayama,* Tatsuya Mizoroki,* Makoto Urushitani,† Yuzuru Imai,† Ryosuke Takahashi,†,[1] Shigeo Murata,‡ Keiji Tanaka‡ and Akihiko Takashima*

**Laboratory for Alzheimer's Disease and †Laboratory for Motor System Neurodegeneration. RIKEN Brain Science Institute, Saitama, Japan*

*‡Department of Molecular Oncology, Tokyo Metropolitan Institute of Medical Science, Tokyo, Japan*

**Abstract**

The carboxyl terminus of heat-shock cognate (Hsc)70-interacting protein (CHIP) is a ubiquitin E3 ligase that can collaborate with molecular chaperones to facilitate protein folding and prevent protein aggregation. Previous studies showed that, together with heat-shock protein (Hsp)70, CHIP can regulate tau ubiquitination and degradation in a cell culture system. Ubiquitinated tau is one component in neurofibrillary tangles (NFTs), which are a major histopathological feature of Alzheimer's disease (AD). However, the precise sequence of events leading to NFT formation and the mechanisms involved remain unclear. To confirm CHIP's role in suppressing NFT formation *in vivo*, we performed a quantitative analysis of CHIP in human and mouse brains. We found increased levels of CHIP and Hsp70 in AD compared with normal controls. CHIP levels in both AD and controls corresponded directly to Hsp90 levels, but not to Hsp70 or Hsc70 levels. In AD samples, CHIP was inversely proportional to sarkosyl-insoluble tau accumulation. In a JNPL3 mouse brain tauopathy model, CHIP was widely distributed but weakly expressed in spinal cord, which was the most prominent region for tau inclusions and neuronal loss. Protein levels of CHIP in cerebellar regions of JNPL3 mice were significantly higher than in non-transgenic littermates. Human tau was more highly expressed in this region of mouse brains, but only moderate levels of sarkosyl-insoluble tau were detected. This was confirmed when increased insoluble tau accumulation was found in mice lacking CHIP. These findings suggest that increases in CHIP may protect against NFT formation in the early stages of AD. If confirmed, this would indicate that the quality-control machinery in a neuron might play an important role in retarding the pathogenesis of tauopathies.

**Keywords:** Alzheimer's disease, carboxyl terminus of heat-shock cognate 70-interacting protein, heat-shock protein, molecular chaperone, neurofibrillary tangle, tau.

*J. Neurochem.* (2005) **94**, 1254–1263.

The carboxyl terminus of heat-shock cognate (Hsc)70-interacting protein (CHIP) is a key molecule in protein quality-control processes that links the ubiquitin–proteasome and chaperone systems (Murata *et al.* 2001). CHIP has the U-box domain that facilitates ubiquitin-conjugating enzyme (E2)-dependent ubiquitination (Hatakeyama *et al.* 2001). CHIP was originally discovered as a co-chaperone with a tetratricopeptide repeat-containing protein that negatively regulates the ATPase and chaperone activities of Hsc70 (Ballinger *et al.* 1999). The biochemical effects of CHIP have been well characterized using cell culture systems. Various molecules have been identified as CHIP substrates, including the glucocorticoid receptor (Connell *et al.* 2001), the misfolded cystic fibrosis transmembrane-conductance regulator (CFTR) (Meacham *et al.* 2001), heat-denatured luciferase (Murata *et al.* 2001), the transmembrane receptor tyrosine kinase ErbB2 (Xu *et al.* 2002)

Received February 16, 2005; revised manuscript received April 10, 2005; accepted April 26, 2005.

Address correspondence and reprint requests to Akihiko Takashima, Laboratory for Alzheimer's Disease, RIKEN Brain Science Institute, Wako-shi, Saitama 351–0198, Japan. E-mail: kenneth@brain.riken.jp

[1]The present address of Ryosuke Takahashi is the Department of Neurology, Graduate School of Medicine, Kyoto University, 54 Kawahara-cho, Shogoin, Sakyo-ku, Kyoto 606-8507, Japan.

*Abbreviations used*: AD, Alzheimer's disease; CFTR, cystic fibrosis transmembrane-conductance regulator; CHIP, carboxyl terminus of heat-shock cognate 70-interacting protein; Hsc, heat-shock cognate; HSF1, heat shock factor 1; Hsp, heat-shock protein; MES, 2-(N-Morpholino) ethanesulfonic Acid; NFT, neurofibrillary tangle; NSE, neuron-specific enolase; PAGE, polyacrylamide gel electrophoresis; PBS, phosphate-buffered saline; PHF, paired helical filaments; PHF-tau, PHF-1 antibody-immunoreactive tau; PMSF, phenylmethylsulfonyl fluoride; SDS, sodium dodecyl sulfate; TBS, Tris-buffered saline; Tg, transgenic.



 

and microtubule-associated protein tau (Petrucelli *et al.* 2004; Shimura *et al.* 2004). We found that CHIP directly mediates tau ubiquitination without heat-shock proteins (Hsps) *in vitro*, preferentially interacts with four-repeat tau, and protects against vulnerability of P301L mutated tau expressing cells (Hatakeyama *et al.* 2004). However, little is known about the biochemical features of CHIP in the brain. Only immunohistochemical analyses have been reported, including those that show anti-CHIP antibody-positive tau inclusions in several tauopathies including Alzheimer's disease (AD), progressive supranuclear palsy, corticobasal degeneration and Pick's disease (Hatakeyama *et al.* 2004; Petrucelli *et al.* 2004), and anti-CHIP antibody-positive Lewy body-like hyaline inclusions in a familial amyotrophic lateral sclerosis mouse model (Urushitani *et al.* 2004).

Tau is a neuronal microtubule-binding protein that normally enhances microtubule stability. However, it can be hyperphosphorylated in pathogenic conditions, and detach from microtubules and accumulate in the neurofibrillary tangles (NFTs) that are one of neuropathological hallmarks of AD (Grundke-Iqbal *et al.* 1986). Despite the suspected role of tau phosphorylation in NFT formation, the precise sequence of events leading to NFT formation and the mechanisms involved remain poorly understood. In addition to tau phosphorylation, other abnormal post-translational modifications have been observed including ubiquitination, glycosylation, glycation, polyamination, nitration and proteolysis (for review, see Gong *et al.* 2005). In most neurodegenerative diseases, anti-ubiquitin antibody- and anti-proteasome antibody-positive inclusions were detected in affected neurons (for review, see Sherman and Goldberg 2001), so the ubiquitin–proteasome may be one mechanism responsible for tau degradation in tauopathies. Various molecular chaperones were also colocalized in protein aggregates that are characteristic of neurodegenerative diseases (for review, see Muchowski and Wacker 2005). CHIP may attenuate NFT formation as a bridging mechanism between molecular chaperones and the ubiquitin–proteasome system.

In the present study, human AD brain, JNPL3 mice (Lewis *et al.* 2000) expressing human P301L mutant tau that is associated with frontotemporal dementia and parkinsonism linked to chromosome 17, and a novel *CHIP* knockout mouse were used to investigate the *in vivo* roles of CHIP in regulating tau ubiquitination, degradation and aggregation. We found increased levels of CHIP in AD brains that were inversely proportional to the amount of accumulated tau. The level of CHIP corresponded with the level of Hsp90 but not with that of Hsp70 or Hsc70. These *in vivo* studies of CHIP biochemistry suggest the existence of a Hsp90–CHIP chaperone system, which plays an ameliorating role in the early stages of tauopathies.

## Materials and methods

### Antibodies

Polyclonal CHIP antibodies (R1) were prepared in rabbits (Imai *et al.* 2002). Antiserum specific for recombinant CHIP with a His-Tag sequence was purchased from Calbiochem (La Jolla, CA, USA). E1 (Kenessey *et al.* 1997), a polyclonal antibody specific to human tau (amino acids 19–33, according to the numbering of a longest isoform of human tau unphosphorylated), was prepared in our laboratory. Polyclonal tau antibody tauC was raised against tau polypeptide corresponding to amino acid residues 422–438. Anti-Tau5 and pS199 (phosphorylation site at Ser199) were purchased from Biosource International (Camarillo, CA, USA). Anti-Tau1 was from Chemicon (Temecula, CA, USA). Monoclonal antibody to tau phosphorylated at ser396/Ser404 (PHF-1) was provided by Dr Peter Davies (Jicha *et al.* 1999). Monoclonal antibodies to Hsp90, Hsp70, β-actin, neuron-specific enolase (NSE) and ubiquitin were purchased from Santa Cruz Biotechnology (Santa Cruz, CA, USA), Chemicon, Sigma (St Louis, MO, USA) Upstate (Charlottesville, VA, USA) and MBL (Nagoya, Japan) respectively. Polyclonal antibody to Hsc70 was purchased from MBL. For western blotting, antibodies were used at the following dilutions in blocking solution: CHIP, 1 : 5000; E1, 1 : 5000; tauC, 1 : 5000; tau1, 1 : 2000; tau5, 1 : 2000; pS199, 1 : 5000; PHF-1, 1 : 2000; Hsp90, 1 : 2000; Hsp70, 1 : 1000; β-actin, 1 : 10 000; NSE, 1 : 1000; ubiquitin, 1 : 500; Hsc70, 1 : 1000.

### Human brain

Temporal cortices from nine AD (AD1 to AD9) and six non-AD controls (C1 to C6) were obtained. They were processed for western blotting as described below. The age, sex and post-mortem intervals of each subject were: AD2, 85 years, male, 10 h; AD3, 77 years, female, 2.5 h; AD4, 66 years, female, 2.5 h; AD5, 79 years, male, 1.5 h; AD7, 66 years, male, 2.5 h; AD8, 60 years, female, 3 h; C1, 57 years, female, 8 h; C2, 69 years, male; C3, 69 years, male; C4, 68 years, male, 6 h; C6, 65 years, female. Information about remaining samples was not available (described in Yan *et al.* 1994).

### JNPL3 mice and littermates

Female hemizygous JNPL3 mice (Tau MI with B6D2F1 background; Taconic Laboratories Germantown, NY, USA) were obtained at 8 weeks of age. JNPL3 mice express the 4R0N isoform of human P301L mutant tau and are characterized as developing NFTs, as well as sarkosyl-insoluble tau in an age-dependent manner (Lewis *et al.* 2001; Sahara *et al.* 2002). Transgenic (Tg) mice and non-Tg littermates were bred by mating hemizygous JNPL3 mice with C57BL/6J Jcl (Clea, Tokyo, Japan). Mice were genotyped for the *tau* transgene by PCR between exons 9 and 13 of human tau cDNA. Animals were housed under controlled conditions with a 12-h day–night cycle. They were killed between 1.5 and 11.6 months after birth. The age ranges of the JNPL3 mice were 1.5 months ($n = 2$), 4–5 months ($n = 2$), 6–7 months ($n = 3$), 8–9 months ($n = 3$) and 10–11 months ($n = 2$). The age ranges of non-Tg mice were 1.5 months ($n = 1$), 4–5 months ($n = 3$), 6–7 months ($n = 2$) and 8–9 months ($n = 3$). Procedures involving animals and their care were approved by the Animal Care and Use Committee of RIKEN.

### Tissue extraction

Mouse brains were separated into eight regions: olfactory bulb, cerebral cortex, hippocampus, diencephalons, midbrain, pons and medulla oblongata, cerebellum and spinal cord. These regions were quickly frozen on dry ice and stored at − 80°C. Each sample was homogenized subsequently in five volumes of Tris-buffered saline (TBS) containing protease and phosphatase inhibitors [25 mM Tris/HCl, pH 7.4, 150 mM NaCl, 1 mM EDTA, 1 mM EGTA, 5 mM sodium pyrophosphate, 30 mM β-glycerophosphate, 30 mM sodium fluoride and 1 mM phenylmethylsulfonyl fluoride (PMSF)]. The homogenates were centrifuged at 27 000 *g* for 15 min at 4°C to obtain a supernatant (TBS sup) and pellet fractions. Pellets were re-homogenized in five volumes of high-salt/sucrose buffer (0.8 M NaCl, 10% sucrose, 10 mM Tris/HCl, pH 7.4, 1 mM EGTA, 1 mM PMSF) and centrifuged as above. The supernatants were collected and incubated with sarkosyl (Sigma; 1% final concentration) for 1 h at 37°C, followed by centrifugation at 150 000 *g* for 1 h at 4°C to obtain salt and sarkosyl-soluble and sarkosyl-insoluble pellets (srk-ppt fractions). To determine the extent of post-mortem protein degradation, hemibrains were kept at room temperature (25°C) for various time intervals (1, 2, 4, 8, 24 and 70 h) after the death of 7-month-old female C57BL/6J mice. As a control, the other hemibrains were quickly frozen in dry ice and stored at − 80°C. Each sample was homogenized in TBS buffer containing protease and phosphatase inhibitors, and was centrifuged at 27 000 *g* for 15 min at 4°C. The supernatants were used for western blot analysis.

### *CHIP* knockout mice

The first six exons of the *CHIP* gene were replaced with a PGK-neo selection cassette by homologous recombination. Germline transfer of the targeted allele was successful. Mice heterozygous at the *CHIP* locus were maintained on a C57BL/6 background. Mice aged 2.5 months (wild type $n = 1$, heterozygous $n = 1$, homozygous $n = 1$) and 18 months (wild type $n = 4$, heterozygous $n = 4$, homozygous $n = 4$) were killed, and hemibrains were quickly frozen on dry ice and stored at − 80°C. As described previously (Ishihara *et al.* 1999; Tanemura *et al.* 2002), tissue extracts were sequentially fractionated with the following buffers: reassembly buffer (RAB; 0.1 M 2-(N-Morpholino)ethanesulfonic Acid (MES), 1 mM EGTA, 0.5 mM $MgSO_4$, 0.75 M NaCl, 0.02 M NaF, 1 mM PMSF and protease inhibitor cocktail, pH 7.0), RAB containing 1 M sucrose, RIPA buffer [50 mM Tris, 150 mM NaCl, 1% NP-40, 5 mM EDTA, 0.5% sodium deoxycholate and 0.1% sodium dodecyl sulfate (SDS), pH 8.0], RIPA buffer containing 1% SDS, and TBS containing 1% SDS. The final pellet was solubilized in 70% formic acid and reconstituted in Laemmli SDS–polyacrylamide gel electrophoresis (PAGE) sample buffer after lyophilization.

### Western blotting

Fractionated tissue extracts were dissolved in sample buffer containing β-mercaptoethanol (0.01%). The boiled extracts were separated by gel electrophoresis on 10% or 4–20% gradient SDS–PAGE gels, and transferred to nitrocellulose membranes (Schleicher & Schuell BioScience, Dassel, Germany). After blocking with a blocking solution containing 5% non-fat milk, 0.1% goat serum and 0.1% Tween-20 in phosphate-buffered saline (PBS), the membranes were incubated with various antibodies, washed to remove excess antibodies, and then incubated with peroxidase-conjugated goat anti-rabbit antibodies (1 : 5000; Jackson ImmunoResearch, West Grove, PA, USA) or anti-mouse IgG (1 : 5000; Jackson ImmunoResearch). Bound antibodies were detected using an enhanced chemiluminescence system, SuperSignal West Pico (Pierce Biotechnology, Rockford, IL, USA). For specificity testing of anti-CHIP antibody, pre-absorption was performed. Recombinant His-tagged CHIP was resuspended in 1% bovine serum albumin, 0.1% goat serum and 0.1% Tween-20 in PBS to a concentration of 40 μg/mL. The solution was added to dilute CHIP antibody to a final dilution of 1 : 5000. The mixture was rotated for 2 h at room temperature, then centrifuged at 12 000 *g* for 5 min. The supernatant was separated from the pellet and used for western blotting. Quantitation and visual analysis of immunoreactivity were performed with a computer-linked LAS-1000 Bio-Imaging Analyzer System (Fujifilm, Tokyo, Japan) using the software program Image Gauge 3.0 (Fujifilm).

### Statistical analysis

The correlation between the levels of CHIP in AD brain and control brain, and between CHIP and Hsp levels, was tested by unpaired *t*-test with Welch correction. The correlation between the level of CHIP and PHF-tau was tested using Pearson correlation. Data were analyzed with InStat for Macintosh, version 3.0a (Graphpad, San Diego, CA, USA). The level of significance was set at $p < 0.05$.

## Results

### Identification of CHIP in brain extracts

CHIP, a 35-kDa cytoplasmic protein, is highly expressed in adult striated muscle with less expression in the pancreas and brain. It is also expressed broadly in tissue culture (Ballinger *et al.* 1999). Polyclonal CHIP antibodies from both laboratory and commercial sources were used for western blotting. Both were raised from full-length CHIP recombinant protein. Samples from human embryonic kidney (HEK)293 cells showed the strongest immunoreactive band with a mobility size of 35 kDa (Fig. 1a). Both mouse and human brain extracts showed a single 35-kDa band in the blot with R1 antibody. This band was absorbed by preincubation of primary antibody with recombinant protein. The blot with the Calbiochem antibody showed a 35-kDa band of the same intensity in each sample, but additional bands were detected. These data suggest that the 35-kDa band was the protein product of *CHIP* and that the R1 antibody is more specific to CHIP than the antibody from Calbiochem. We also detected doublet bands in human materials using the enlarged electrophoretic condition (Fig. 1b). For quantitative analysis, we excluded the upper band in human materials because the mobility of the lower band was same as the 35-kDa band in mouse brain (Fig. 1b) and all the human brain samples showed similar extensions of the upper band (Fig. 2a).

### Levels of CHIP in AD brain were higher than levels in non-AD controls

Quantitative western blotting analyses revealed variable levels of the 35-kDa band in human brain extracts (Fig. 2a).

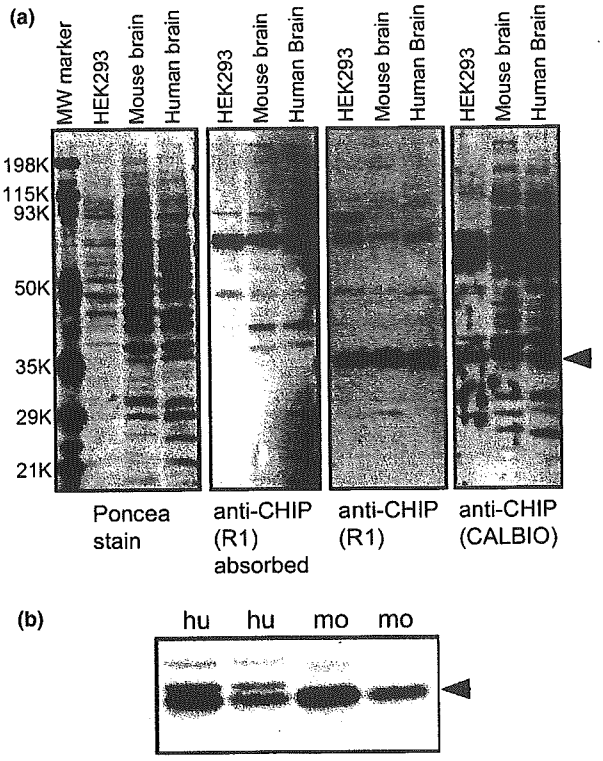


**Fig. 1** Identification of CHIP using specific antibodies. (a) Replicated membranes containing human embryonic kidney (HEK)293 cells, mouse brain and human brain extracts were immunoblotted with anti-CHIP antibodies [preabsorbed R1, R1 and Calbiochem (CALBIO)]. One set of membranes was stained with poncea. A 35-kDa band (arrowhead) was detected with both R1 and Calbiochem antibodies but completely absorbed by recombinant CHIP. (b) Human brain extracts contained doublet bands. The lower band in human brain indicated by arrowhead was identical to the band in mouse brain.

Before making comparisons between AD and non-AD controls, both sarkosyl-insoluble tau and SDS-insoluble β-amyloid were analyzed by western blotting to confirm diagnostic information. PHF-1-positive triplet bands were detected in all nine AD cases but not in the non-AD controls when sarkosyl-insoluble fractions derived from over 40 mg wet-weight of brain tissue were loaded (data not shown). SDS-insoluble β-amyloid was detected in all AD cases and some non-AD controls (data not shown). To compare protein levels of CHIP and Hsp between AD and non-AD controls, the amount of β-actin was used for normalization of protein levels. Levels of CHIP were significantly higher in AD brain compared with non-AD controls ($p = 0.040$; unpaired $t$-test with Welch correction) (Fig. 2b). A significant increase in Hsp70 levels in AD compared with control brains was observed ($p = 0.0032$) (Fig. 2d), but no significant difference in either Hsp90 or Hsc70 ($p = 0.84$ and $p = 0.57$ respectively) (Fig. 2c). Comparing individual samples, CHIP and Hsp90 levels were directly related, but CHP levels were not related to those of either Hsp70 or Hsc70 (Figs 2a and e). The correlation between the levels of CHIP and Hsp90 was highly significant ($r = 0.71$, $p = 0.0029$, $n = 15$; Pearson correlation). When the amount of NSE was used for normalization, the same statistical results were obtained (data not shown).

### Inverse relationship between CHIP and PHF-1 antibody-immunoreactive tau (PHF-tau) in AD brain

To determine whether NFT formation in AD brain is influenced by the protein level of CHIP, the amount of CHIP, normalized with respect to β-actin in the TBS-soluble fraction, was plotted against PHF-tau in the sarkosyl-insoluble fraction. These were samples that tested positive for highly phosphorylated tau. Although detailed information on the pathological course for each AD case was not available, the relative amount of PHF-tau revealed through biochemical studies provided detailed information about the NFT pathogenesis in each. This information correlated with the severity of disease (Dickson *et al.* 2000; Johnson and Bailey 2002). As shown in Fig. 2(a), the intensity of PHF-tau staining varied among the AD cases as did that of both CHIP and Hsp90. Interestingly, the amount of PHF-tau was inversely proportional to amount of CHIP ($r = -0.83$, $p = 0.0051$, $n = 9$; Pearson correlation) (Fig. 2f). As described previously, levels of Hsp90 in AD cases with mature PHF-tau accumulation were lower than those in immature or non-AD cases (Dou *et al.* 2003). Conversely, soluble tau levels were not influenced by either CHIP or Hsp90 levels. To determine whether the sequestration of CHIP with NFTs occurred during pathogenesis, we analyzed CHIP levels in the sarkosyl-insoluble fraction (Fig. 2a). Consistent with the results of the anti-CHIP blot of the TBS sup fraction, the level of sarkosyl-insoluble CHIP was inversely related to the PHF-tau level. Sarkosyl-insoluble CHIP in controls was also detected with similar intensity to that in AD cases. These data suggest that CHIP precipitated in this fraction in a PHF-tau-independent manner.

### Effect of post-mortem interval on protein levels of CHIP

Large variations in CHIP and Hsp90 protein levels were found among control and AD brains (Fig. 2a). To exclude the possibility of post-mortem protein degradation, we attempted the comparative protein quantification of mouse brains with several post-mortem intervals. Coomassie Brilliant Blue staining of polyacrylamide gels showed visible protein degradation after a post-mortem interval of 24 h (Fig. 3). However, western blots for CHIP, Hsp90, Hsp70 and β-actin showed constant protein levels. Only tau protein levels were affected by the post-mortem interval. The observed mobility shift may correspond to dephosphorylation. These data strongly suggest that protein levels of CHIP and Hsps extracted from both human and mouse brains were not affected by the post-mortem interval.

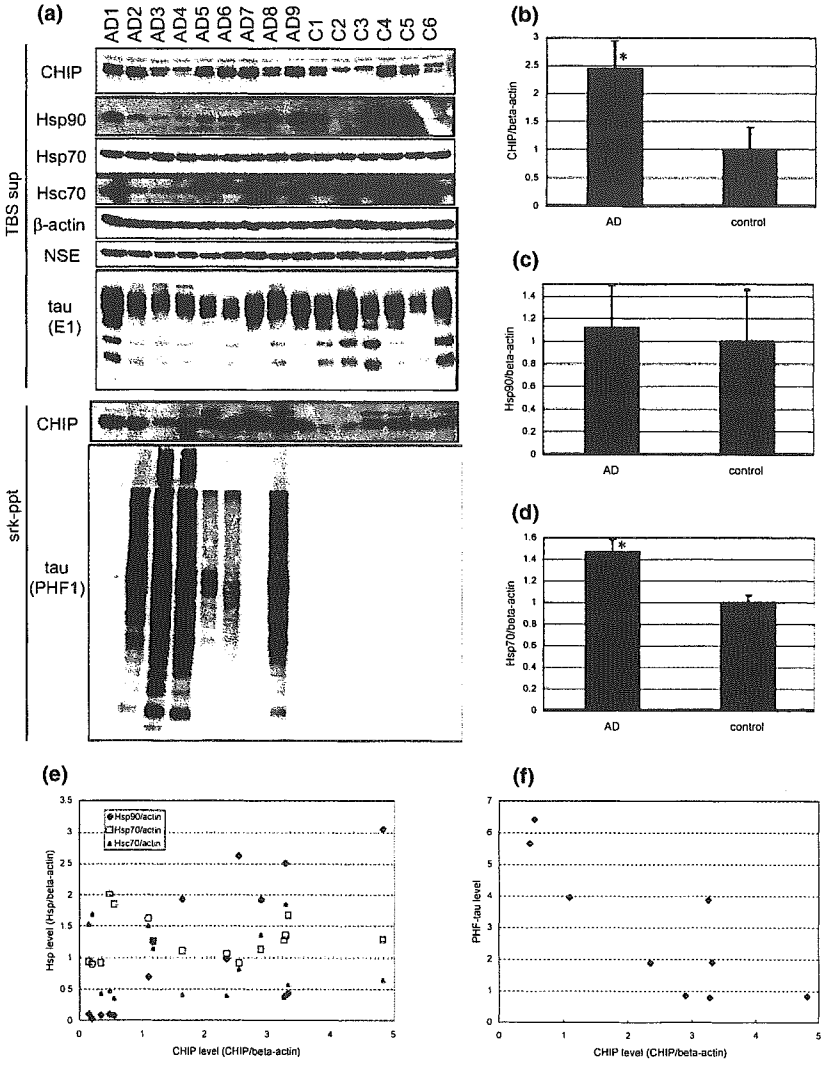


**Fig. 2** Quantitative analysis of CHIP in human brains. (a) TBS-soluble fractions (TBS sup) from human temporal cortex from nine AD and six non-AD control cases were blotted using CHIP (R1), Hsp90, Hsp70, Hsc70, β-actin, NSE and E1 antibodies. Sarkosyl-insoluble fractions (srk-ppt) derived from 40 mg wet-weight of brain were blotted using CHIP (R1) antibodies and those derived from 4 mg wet-weight of brain were blotted using PHF-1 antibody. Amounts of CHIP (b), Hsp90 (c) and Hsp70 (d) normalized with respect to β-actin were analyzed. Values are mean ± SEM. $^*p < 0.05$ versus control (unpaired *t*-test with Welch correction). (e) Correlations between CHIP and Hsp90, Hsp70 or Hsc70 levels. (f) Amount of CHIP normalized with respect to β-actin in TBS-soluble fraction plotted against sarkosyl-insoluble PHF-tau level. $p < 0.01$ ($n = 9$; Pearson correlation).

### Distribution of CHIP in mouse brain

Since the discovery of CHIP (Ballinger *et al.* 1999) and its role as E3 ligase (Hatakeyama *et al.* 2001; Jiang *et al.* 2001; Murata *et al.* 2001), little research has been conducted to determine its *in vivo* protein properties. In the present study the distribution of CHIP in mouse brain was investigated using biochemical strategies. CHIP was found to be highly expressed in the olfactory bulb, cerebral cortex, hippocampus and cerebellum, moderately expressed in the diencephalons, midbrain and pons/medulla oblongata, but weakly expressed in the spinal cord (Fig. 4a). Hsp90 was broadly expressed throughout the mouse brain, whereas Hsp70 was highly expressed in cerebral cortex and hippocampus with only moderate expression in other brain regions (Fig. 4a). The distribution patterns of the three chaperone-related proteins in mouse samples were not identical. CHIP distribution in mouse brain corresponded with tau distribution except in the olfactory bulb. The distribution patterns of CHIP, Hsp90 and Hsp70 did not vary with age or sex (data not shown).

### Increased level of CHIP in JNPL3 mouse brain

To search for linkages between abnormal tau accumulation and CHIP expression, JNPL3 mouse brains were analyzed; 64-kDa tau was observed in the sarkosyl-insoluble fraction from the midbrain, pons/medulla oblongata and spinal cord regions of 9.5-month-old female JNPL3 mouse (Fig. 4b, middle panel). As described previously (Sahara *et al.* 2002), human P301L tau protein expression was higher in the hindbrain regions, including midbrain, pons/medulla oblongata, cerebellum and spinal cord, than in the forebrain regions, including cerebral cortex, hippocampus and diencephalons (Fig. 4b, upper panel). Interestingly, the cerebellum had the highest levels of exogenous tau protein but only moderate levels of sarkosyl-insoluble tau. The distribution pattern of

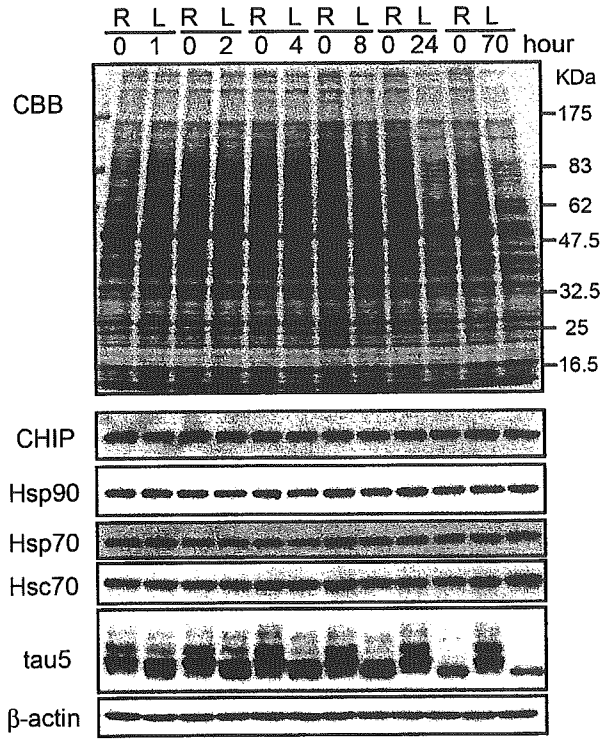


**Fig. 3** Effect of post-mortem interval on protein degradation in mouse brains. TBS-soluble fractions from mouse hemibrains were separated by SDS–PAGE then immunoblotted using CHIP, Hsp90, Hsp70, Hsc70, tau5 and β-actin antibodies. One hemibrain (R) was quickly frozen and stored at − 80°C (post-mortem interval zero). The other (L) was kept at room temperature for 1, 2, 4, 8, 24 or 70 h after death. Equal volumes of samples derived from 0.33 mg wet-weight tissue were resolved by SDS–PAGE. Upper panel shows Coomassie Brilliant Blue (CBB) staining with molecular weight markers.

CHIP in JNPL3 mouse brain was similar to that in wild type (compare Fig. 4b with Fig. 4a). The level of CHIP in spinal cord was only 20% of that in cerebellum. The level of sarkosyl-insoluble tau was inversely related to CHIP levels in cerebellum and spinal cord. Because amounts of sarkosyl-insoluble tau were inversely related to the amount of CHIP in AD brains, we checked the CHIP levels in both cerebellum and spinal cord regions. CHIP levels were more than 15% higher in JNPL3 mouse cerebellar regions than those in non-Tg mouse cerebellar regions, but no difference was found in the levels in the spinal cords of JNPL3 and non-Tg mice when protein levels were normalized with respect to β-actin (cerebellum, $p = 0.023$; spinal cord, $p = 0.49$) (Fig. 4c). Neuronal loss in the spinal cord of JNPL3 mice (Lewis *et al.* 2000) was confirmed by checking the protein levels of NSE as a marker. As shown in Fig. 4(e), the NSE level was significantly lower in JNPL3 mouse spinal cord ($p = 0.0035$). When CHIP levels were normalized with respect to NSE, the levels in JNPL3 mouse spinal cords were higher than those in non-Tg mouse spinal cords but the difference was not significant different ($p = 0.10$) (Fig. 4d).

As the development of tau pathology in the JNPL3 mouse is age dependent, we checked the levels of both CHIP and Hsp90 at different ages. By 11 months of age, the CHIP level in spinal cord was slightly increased but the Hsp90 level was not (Fig. 5a). In cerebellum, no significant differences in either CHIP or Hsp90 levels were found during ageing (Fig. 5b). Although 64-kDa tau was detected in JNPL3 mouse cerebellum, the accumulation of sarkosyl-insoluble tau in spinal cord was greater than that in cerebellum. These data suggest that overexpression of P301L tau increases the amount of CHIP which then attenuates NFT formation, although sufficient levels of CHIP are not produced in spinal cord.

### Increased level of insoluble tau in aged *CHIP–/–* mouse brain

Unlike the CHIP-deficient mice described by Dai *et al.* (2003), our *CHIP–/–* mice showed significant anatomical abnormalities such as lower bodyweight and dysbasia. Some 95% of *CHIP–/–* mice die by the third week after birth. The remaining mice survive for more than 1 year. These phenotypes might be due to their genetic backgrounds because our heterozygous mice were maintained on a C57BL/6 strain and back-crossed over five times (Murata S. *et al.*, unpublished observation). We first analyzed the involvement of CHIP in tau phosphorylation and degradation using 2.5- and 18-month-old mouse brains. There were no significant differences in the amounts of soluble tau or tau phosphorylation between wild-type and CHIP-deficient mice (Fig. 6a). We analyzed the solubility of tau protein by extracting brains using buffers with increasing extraction strengths to determine whether tau becomes insoluble in CHIP-deficient mice. Interestingly, both aged *CHIP–/–* and heterozygous (*CHIP+/–*) mouse brains showed increased levels of SDS-insoluble tau, detected by both phosphorylation-independent and -dependent tau antibodies (Fig. 6a). Three additional 18-month-old *CHIP–/–*, *CHIP+/–* and *CHIP+/+* mouse brains were analyzed for insoluble tau accumulation. Although the amount of SDS-insoluble tau varied, it tended to increase with greater CHIP deficiency (Fig. 6c). When we quantified the protein levels of CHIP, heterozygous mouse brains had only 6% of that found in wild-type mouse brains (Fig. 6b). These data suggest that suppression of CHIP induces abnormal tau accumulation in a phosphorylation-independent manner in aged mice.

## Discussion

Previous studies have linked CHIP with tau ubiquitination and degradation (Hatakeyama *et al.* 2004; Petrucelli *et al.* 2004; Shimura *et al.* 2004). In this report, we describe the biochemical features of CHIP in human and mouse brain. An

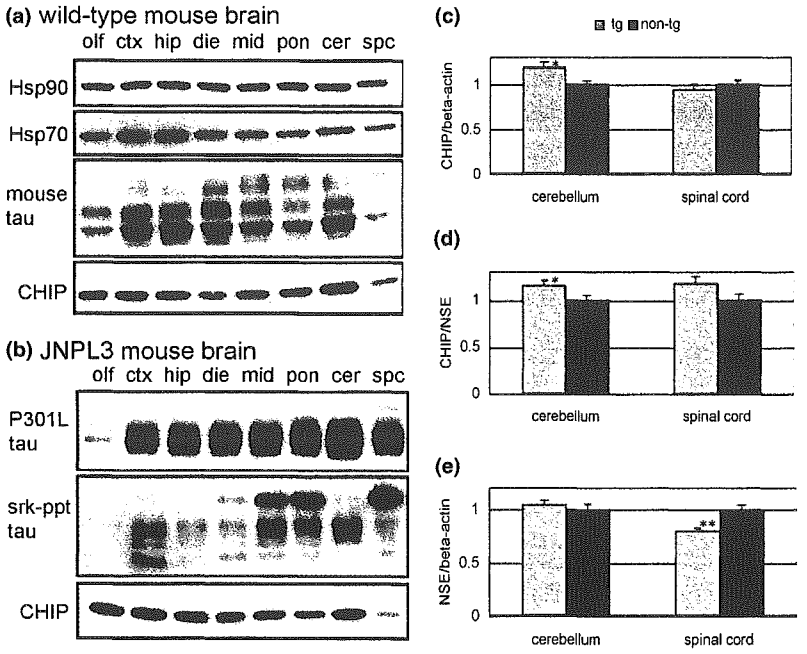


**Fig. 4** CHIP distribution in wild-type and JNPL3 mouse brain. (a) TBS-soluble fractions prepared from olfactory bulb (olf), cerebral cortex (ctx), hippocampus (hip), diencephalons (die), midbrain (mid), pons and medulla oblongata (pon), cerebellum (cer) and spinal cord (spc) of 9.3-month-old female mouse were immunoblotted using Hsp90, Hsp70, tau5 and CHIP (R1) antibodies. Equal volumes of samples based on wet weight was resolved by SDS–PAGE. (b) TBS-soluble fractions prepared from the same regions of 9.3-month-old female JNPL3 mouse were blotted using E1 and CHIP (R1) antibodies (top and bottom panel respectively). Sarkosyl-insoluble fractions (srk-ppt) derived from 5 mg wet-weight of each brain region was blotted using E1 antibody (middle). Amounts of CHIP normalized with respect to β-actin (c) and NSE (d), and NSE normalized with respect to β-actin, in cerebellum and spinal cord from Tg (4–10-month-old females, $n = 8$) and non-Tg littermates (females, $n = 8$). Values are mean ± SEM. $^{*}p < 0.05$, $^{**}p < 0.01$ versus non-Tg (unpaired *t*-test with Welch correlation).

increased level of CHIP in AD brain, with respect to controls, was observed. When we analyzed individual differences, the protein levels of CHIP corresponded with Hsp90 levels. An inverse relationship between tau aggregation and CHIP levels was observed in humans and in our mice with tauopathy. We found that a lack of CHIP influenced insoluble tau accumulation. These data suggest that CHIP may protect against tau aggregation and NFT formation.

CHIP is a ubiquitin protein ligase that selectively ubiquitinates denatured proteins when the substrate is captured by a molecular chaperone, including Hsp90 or Hsc70 (Murata *et al.* 2001). Involvement of Hsc70 in the CHIP-dependent ubiquitination of CFTR was also reported (Meacham *et al.* 2001). Connell *et al.* (2001) noted that the ubiquitination-dependent instability of the Hsp90-trapped glucocorticoid receptor was promoted by CHIP. Dai *et al.* (2003) reported that CHIP regulates the activation of Hsp70 by inducing trimerization and transcriptional activation of heat shock factor 1 (HSF-1). Petrucelli *et al.* (2004) found that Hsp70 could reduce tau levels in both a cell culture system and mouse brain. We present novel evidence that levels of Hsp90 correspond to CHIP levels in aged human brains. As Hsp90 often pairs with Hsc/Hsp70, the two chaperones are often thought to be part of a single multichaperone machine (for review, see Young *et al.* 2001), but accumulating evidence suggests that both also work alone. In addition to our CHIP/Hsp90 response, up-regulation of Hsp70 in AD brains has also been reported (Yoo *et al.* 1999). This suggests that in the human brain CHIP might modulate this machinery by interacting directly, and specifically, with either protein in response to the nature of protein misfolding and aggregation.

Immunohistochemical studies found CHIP co-localized with tau-positive lesions in neurons and glia (Petrucelli *et al.* 2004). The number of CHIP-immunoreactive lesions was 50–70% for Pick's disease, 5–10% for AD and 1–5% for both progressive supranuclear palsy and corticobasal degeneration in these studies when CHIP was confirmed using a CHIP-specific antibody with peptide pre-absorption. In contrast, we reported that anti-CHIP antibody stained NFT-bearing cells in progressive supranuclear palsy brain, but only faintly in AD (Hatakeyama *et al.* 2004). This discrepancy might be due to the different specificities of the antibodies. We produced CHIP antibodies from recombinant proteins and confirmed their specificity by western blotting (Fig. 1). Our biochemical observation showed that the amounts of sarkosyl-insoluble tau did not correspond to

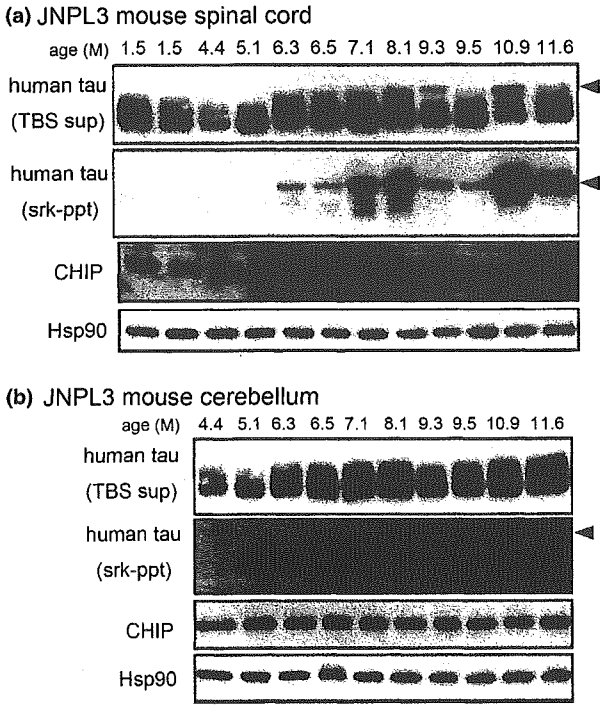


**Fig. 5** Changes in CHIP and Hsp90 levels in JNPL3 mouse spinal cord and cerebellum with age. (a) Samples from spinal cords of 1.5–11.6-month (M)-old female JNPL3 mice were analyzed. TBS-soluble fractions (TBS sup) were immunoblotted using E1, CHIP and Hsp90 antibodies. The second panel from the top shows sarkosyl-insoluble fractions (srk-ppt) blotted with E1 antibody (note that the exposure time was shorter than that used for middle panel of Fig. 4b). Equal volumes, based on wet weight, of each sample were resolved by SDS–PAGE. The 64-kDa band (arrowhead) was detected by the E1 antibody in both TBS sup and srk-ppt. (b) Samples from cerebellum of 4.4–11.6-month-old female JNPL3 mice. TBS-soluble fractions (TBS sup) were immunoblotted using E1, CHIP and Hsp90 antibodies. The second panel from the top shows sarkosyl-insoluble fractions (srk-ppt) blotted with E1 antibody (note that the exposure time was much longer than for second panel from top in Fig. 5a).

CHIP levels in NFT-enriched fractions (Fig. 2a). If a direct association between CHIP and Hsp90 can be confirmed, the previous report showing an inverse relationship between aggregated tau and the level of Hsp90 in tau Tg mice and AD brains (Dou *et al.* 2003) will support our observations. The reduction in the levels of CHIP/Hsp90 may stem from the degradation of these proteins together with maturing tau aggregation by a lysosomal pathway or other mechanism. Although more precise experiments are required to confirm the sequestration of CHIP with tau inclusions, we suspect that CHIP expression is up-regulated to cooperate with molecular chaperones for suppression of NFT formation at the early stage of AD.

Here, we quantified CHIP levels in JNPL3 mouse brains in which P301L tau is overexpressed. We observed increased levels of CHIP in the cerebellar regions of JNPL3 mice when compared with age-matched non-Tg littermates and that cerebellar regions of JNPL3 mice had less sarkosyl-insoluble tau than spinal cords, whereas the total tau levels in cerebellum were higher than those in spinal cords (Fig. 4). The finding that the cerebellum had less sarkosyl-insoluble tau than the spinal cord does not contradict the original observations of the pathological features in JNPL3 mouse brain (Lewis *et al.* 2001). We observed that age-dependent hyperphosphorylated tau accumulation in cerebellum of JNPL3 mice was delayed (Fig. 5). In AD, NFTs are observed in the hippocampus and neocortex but not the cerebellum (Larner 1997). Previously, we reported that hyperphosphorylation of tau after changes in glucose metabolism was lower in the cerebellum than in the hippocampus and cerebral cortex (Planel *et al.* 2004). Both CHIP expression and resistance of tau hyperphosphorylation may attenuate abnormal tau accumulation in mouse cerebellum. Because an inverse accumulation of sarkosyl-insoluble tau with CHIP levels, but not Hsp levels, was observed in the mouse brain, CHIP might be essential in preventing prevent tau aggregation whereas Hsp90 and Hsp70 have additional functions in many cellular processes, including protein folding, transport, degradation and signal transduction. The inconsistency between humans and mice might be explained by brain regional differences. To determine whether Hsp90 cooperates with CHIP to prevent tau aggregation in mouse brain, a model that develops tau pathology in cerebral cortex such as the human P301S tau Tg mouse would be more useful (Allen *et al.* 2002). In contrast to human AD brains, which showed massive accumulation of PHF-tau and reduced levels of CHIP, we found no reduction in CHIP levels in either cerebellum or spinal cord of aged JNPL3 mice. It is possible that unknown ubiquitin ligases other than CHIP might be reduced in these brain regions. Further studies are necessary to determine what other factors might be responsible for tau aggregation in JNPL3 mice.

The biochemical analysis of tau in the *CHIP* knockout mouse brains revealed a slight increase in detergent-insoluble tau with no change in the total amount of tau. This indicates that, although eliminating CHIP is not sufficient to induce NFT formation, a lack of CHIP is involved is NFT formation when tau abnormalities are present. As the precise roles of the chaperone system and the ubiquitin proteasomal system within the pathogenesis of tauopathies have yet to be determined, cross-breeding the *CHIP* knockout mouse with a tau Tg mouse may be beneficial.

To our knowledge, this is the first *in vivo* study of CHIP's properties. We confirmed that co-chaperone CHIP was up-regulated by early NFT formation and prevented tau aggregation with the help of molecular chaperones in human and mouse brains. Therefore, CHIP can modify the disease states of human tauopathies when working in combination with its molecular chaperones.

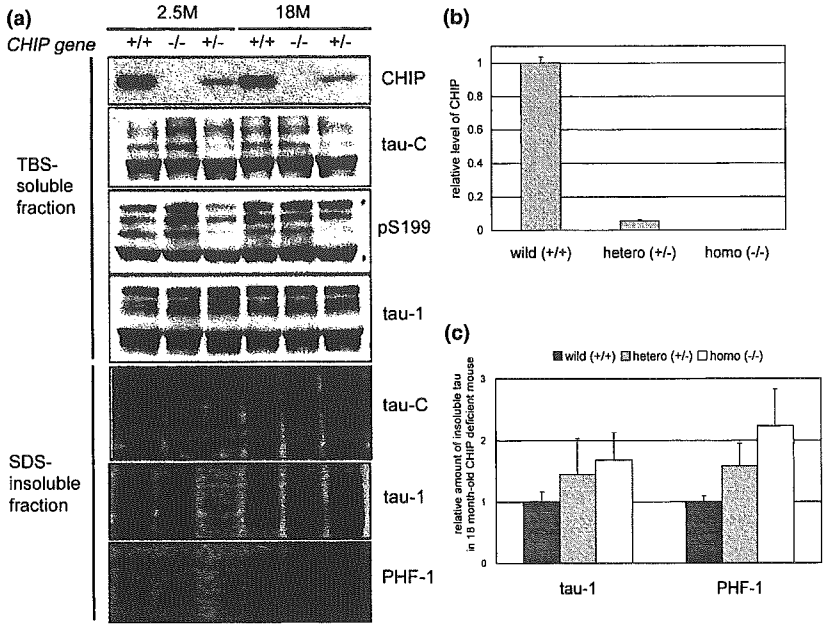


**Fig. 6** Insoluble tau accumulation in *CHIP* knockout mouse brain. (a) TBS-soluble fractions derived from 2.5- and 18-month (M)-old *CHIP*+/+, *CHIP*+/– and *CHIP*–/– mouse brains were immunoblotted using CHIP (R1), tauC, pS199 and tau-1 antibodies. SDS-insoluble fractions extracted with 70% formic acid were immunoblotted using tauC, tau1 and PHF-1 antibodies. Samples containing equal amounts of protein were resolved by SDS–PAGE. (b) Relative levels of CHIP in 18-month-old mouse brains ($n = 3$). Values are mean ± SEM with respect to levels in wild-type mice. (c) Amounts of insoluble tau in 18-month-old mouse brains ($n = 3$). SDS-insoluble fractions extracted with 70% formic acid were immunoblotted using tau1 and PHF-1 antibodies, then quantified by means of an image analyzer. Values are mean ± SEM with respect to levels in wild-type mice.

## Acknowledgements

This work was supported by research grants from RIKEN Brain Science Institute and a Grant-in-Aid for Scientific Research (Japan Ministry of Education, Culture, Sports, Science and Technology). We are grateful to Bonnie Lee La Madeleine for editing this manuscript.

## References

Allen B., Ingram E., Takao M. *et al.* (2002) Abundant tau filaments and nonapoptotic neurodegeneration in transgenic mice expressing human P301S tau protein. *J. Neurosci.* **22**, 9340–9351.

Ballinger C. A., Connell P., Wu Y., Hu Z., Thompson L. J., Yin L. Y. and Patterson C. (1999) Identification of CHIP, a novel tetratricopeptide repeat-containing protein that interacts with heat shock proteins and negatively regulates chaperone functions. *Mol. Cell. Biol.* **19**, 4535–4545.

Connell P., Ballinger C. A., Jiang J., Wu Y., Thompson L. J., Hohfeld J. and Patterson C. (2001) The co-chaperon CHIP regulates protein triage decisions mediated by heat-shock proteins. *Nat. Cell Biol.* **3**, 93–96.

Dai Q., Zhang C., Wu Y. *et al.* (2003) CHIP activates HSF1 and confers protection against apoptosis and cellular stress. *EMBO J.* **22**, 5446–5458.

Dickson D. W., Lin W. K., Ksiezak-Reding H. and Yen S.-H. (2000) Neuropathologic and molecular considerations. *Adv. Neurol.* **82**, 9–27.

Dou F., Netzer W. J., Tanemura K., Li F., Hartl F. U., Takashima A., Gouras G. K., Greengard P. and Xu H. (2003) Chaperons increase association of tau protein with microtubules. *Proc. Natl Acad. Sci. USA* **100**, 721–726.

Gong C.-X., Liu F., Grundke-Iqbal I. and Iqbal K. (2005) Post-translational modification of tau protein in Alzheimer's disease. *J. Neural. Transm.* **112**, 813–838.

Grundke-Iqbal I., Iqbal K., Quinlan M., Tung Y. C., Zaidi M. S. and Wisniewski H. M. (1986) Microtubule-associated protein tau: a component of Alzheimer-paired helical filaments. *J. Biol. Chem.* **261**, 6084–6089.

Hatakeyama S., Yada M., Matsumoto M., Ishida N. and Nakayama K. I. (2001) U box proteins as a new family of ubiquitin-protein ligases. *J. Biol. Chem.* **276**, 33111–33120.

Hatakeyama S., Matsumoto M., Kamura T., Murayama M., Chui D.-H., Planel E., Takahashi R., Nakayama K. I. and Takashima A. (2004) U-box protein carboxyl terminus of Hsc70-interacting protein (CHIP) mediates poly-ubiquitylation preferentially on four-repeat tau and is involved in neurodegeneration of tauopathy. *J. Neurochem.* **91**, 299–307.

Imai Y., Soda M., Hatakeyama S., Akagi T., Hashikawa T., Nakayama K. and Takahashi R. (2002) CHIP is associated with Parkin, a gene responsible for familial Parkinson's disease, and enhances its ubiquitin ligase activity. *Mol. Cell* **10**, 55–67.

Ishihara T., Hong M., Zhang B., Nakagawa Y., Lee M. K., Trojanowski J. Q. and Lee V. M.-Y. (1999) Age-dependent emergence and progression of a tauopathy in transgenic mice overexpressing the shortest human tau isoform. *Neuron* **24**, 751–762.

Jiang J., Ballinger C. A., Wu Y., Dai Q., Cyr D. M., Hohfeld J. and Patterson C. (2001) CHIP is a U-box-dependent E3 ubiquitin ligase: identification of Hsc70 as a target for ubiquitylation. *J. Biol. Chem.* **276**, 42938–42944.

Jicha G. A., Berenfeld B. and Davies P. (1999) Sequence requirements for formation of conformational variants of tau similar to those found in Alzheimer's disease. *J. Neurosci. Res.* **55**, 713–723.

Johnson G. V. and Bailey C. D. (2002) Tau, where are we now? *J. Alzheimers Dis.* **4**, 375–398.

Kenessey A., Nacharaju P., Ko L.-W. and Yen S.-H. (1997) Degradation of tau by lysosomal enzyme cathepsin D: implication for Alzheimer neurofibrillary degeneration. *J. Neurochem.* **69**, 2026–2038.

Larner A. J. (1997) The cerebellum in Alzheimer's disease. *Dement. Geriatr. Cogn. Disord.* **8**, 203–209.

Lewis J., McGowan E., Rockwood J. *et al.* (2000) Neurofibrillary tangles, amyotrophy and progressive motor disturbance in mice expressing mutant (P301L) tau protein. *Nat. Genet.* **25**, 402–405.

Lewis J., Baker M., Van Slegtenhorst M. and Hutton M. (2001) Molecular genetics and transgenic modeling of the tauopathies in Alzheimer's disease, in *Advances in Etiology, Pathogenesis and Therapeutics* (Iqbal K., Sisodia S. S., Winblad B., eds), pp. 71–85. Jon Wiley & Sons, Chichester.

Meacham G., Patterson C., Zhang W., Younger J. M. and Cyr D. M. (2001) The Hsc70 co-chaperone CHIP targets immature CFTR for proteasomal degradation. *Nat. Cell Biol.* **3**, 100–105.

Muchowski R. J. and Wacker J. L. (2005) Modulation of neurodegeneration by molecular chaperones. *Nat. Rev.* **6**, 11–22.

Murata S., Minami Y., Minami M., Chiba T. and Tanaka K. (2001) CHIP is a chaperone-dependent E3 ligase that ubiquitylates unfolded protein. *EMBO Report* **2**, 1133–1138.

Petrucelli L., Dickson D., Kehoe K. *et al.* (2004) CHIP and Hsp70 regulate tau ubiquitination, degradation and aggregation. *Hum. Mol. Genet.* **13**, 703–714.

Planel E., Miyasaka T., Launey T., Chui D.-H., Tanemura K., Sato S., Murayama O., Ishiguro K., Tatebayashi Y. and Takashima A. (2004) Alterations in glucose metabolism induce hypothermia leading to tau hyperphosphorylation through differential inhibition of kinase and phosphatase activities: implications for Alzheimer's disease. *J. Neurosci.* **24**, 2401–2411.

Sahara N., Lewis J., DeTure M., McGowan E., Dickson D. W., Hutton M. and Yen S.-H. (2002) Assembly of tau in transgenic animals expressing P301L tau: alteration of phosphorylation and solubility. *J. Neurochem.* **83**, 1498–1508.

Sherman M. Y. and Goldberg A. L. (2001) Cellular defenses against unfolded proteins: a cell biologist thinks about neurodegenerative diseases. *Neuron* **29**, 15–32.

Shimura H., Schwartz D., Gygi S. P. and Kosik K. S. (2004) CHIP–Hsc70 complex ubiquitinates phosphorylated tau and enhances cell survival. *J. Biol. Chem.* **279**, 4869–4876.

Tanemura K., Murayama M., Akagi T., Hashikawa T., Tominaga T., Ichikawa M., Yamaguchi H. and Takashima A. (2002) Neurodegeneration with tau accumulation in a transgenic mouse expressing V337M human tau. *J. Neurosci.* **22**, 133–141.

Urushitani M., Kurisu J., Tateno M., Hatakeyama S., Nakayama K., Kato S. and Takahashi R. (2004) CHIP promotes proteasomal degradation of familial ALS-linked mutant SOD1 by ubiquitinating Hsp/Hsc70. *J. Neurochem.* **90**, 231–244.

Xu W., Marcu M., Yuan X., Mimnaugh E., Patterson C. and Neckers L. (2002) Chaperone-dependent E3 ubiquitin ligase CHIP mediates a degradative pathway for c-ErbB2/Neu. *Proc. Natl Acad. Sci. USA* **99**, 12847–12852.

Yan S.-D., Chen X., Schmidt A.-M. *et al.* (1994) Glycated tau protein in Alzheimer disease: a mechanism for induction of oxidative stress. *Proc. Natl Acad. Sci. USA* **91**, 7787–7791.

Yoo B. C., Seidl R., Cairns N. and Lubec G. (1999) Heat-shock protein 70 levels in brain of patients with Down syndrome and Alzheimer's disease. *J. Neural Transm. Suppl.* **57**, 315–322.

Young J. C., Moarefi I. and Hartl F. U. (2001) Hsp90: a specialized but essential protein-folding tool. *J. Cell Biol.* **154**, 267–273.

 

# LETTERS

# A heterodimeric complex that promotes the assembly of mammalian 20S proteasomes

Yuko Hirano[1], Klavs B. Hendil[2], Hideki Yashiroda[1], Shun-ichiro Iemura[3], Ryoichi Nagane[3], Yusaku Hioki[3], Tohru Natsume[3], Keiji Tanaka[1] & Shigeo Murata[1,4]

**The 26S proteasome is a multisubunit protease responsible for regulated proteolysis in eukaryotic cells[1,2]. It comprises one catalytic 20S proteasome and two axially positioned 19S regulatory complexes[3]. The 20S proteasome is composed of 28 subunits arranged in a cylindrical particle as four heteroheptameric rings, $\alpha_{1-7}\beta_{1-7}\beta_{1-7}\alpha_{1-7}$ (refs 4, 5), but the mechanism responsible for the assembly of such a complex structure remains elusive. Here we report two chaperones, designated proteasome assembling chaperone-1 (PAC1) and PAC2, that are involved in the maturation of mammalian 20S proteasomes. PAC1 and PAC2 associate as heterodimers with proteasome precursors and are degraded after formation of the 20S proteasome is completed. Overexpression of PAC1 or PAC2 accelerates the formation of precursor proteasomes, whereas knockdown by short interfering RNA impairs it, resulting in poor maturation of 20S proteasomes. Furthermore, the PAC complex provides a scaffold for α-ring formation and keeps the α-rings competent for the subsequent formation of half-proteasomes. Thus, our results identify a mechanism for the correct assembly of 20S proteasomes.**

It is presumed that assembly of 20S proteasomes starts by the spontaneous formation of α-rings[6–8]; however, the exact mechanism responsible for α-ring formation remains elusive. Seven β-subunits, some of which are in precursor forms, are arranged on the α-ring to form a complex named the 'half-proteasome', which consists of one α-ring, one β-ring and the chaperone protein Ump1. To complete maturation of the 20S proteasome, two half-proteasomes dimerize, the propeptides of β-subunits are removed and Ump1 is degraded[9–14]. This model is based mainly on studies in yeast. In mammals, POMP or Proteassemblin, a homologue of yeast Ump1 referred to here as human Ump1 (hUmp1), is also implicated in assembly of 20S proteasomes[15–17]. However, the biogenesis of 20S proteasomes remains largely elusive, especially in mammalian cells.

To identify proteins that interact with mammalian proteasomes, β1i subunits with a Flag tag were expressed in cells and anti-Flag immunoprecipitates were analysed by liquid chromatography coupled with tandem mass spectrometry[18]. We identified hUmp1 in addition to almost all of the subunits of 20S proteasomes and 19S regulatory complexes. We also identified two molecules with previously unknown relevance to proteasomes. One was Down syndrome critical region 2 (DSCR2), a small leucine-rich protein of 288 amino acids[19] that we have renamed PAC1. The other was a protein of 264 amino acids known as hepatocellular carcinoma associated gene 3 (HCCA3) (ref. 20), which we have renamed PAC2. Both PAC1 and PAC2 are ubiquitously expressed in mammals[19,20].

First, we confirmed that these molecules interact physically with proteasomes by transfecting Flag–PAC1 or Flag–PAC2 into HEK293T cells. The association increased on treatment of the cells with MG132, a proteasome inhibitor, in line with the increase in PAC1 and PAC2 expression (Supplementary Fig. 1a). Next, extracts of HeLa cells stably expressing Flag–PAC1 or Flag–PAC2 were fractionated by 8–32% glycerol gradient centrifugation. Both Flag–PAC1 and Flag–PAC2 were observed mainly in fractions containing sediments of precursor forms of proteasomes, as shown by the co-sedimentation of hUmp1, the unprocessed β1i (pro-β1i) subunit and α-subunits, and by the lack of chymotrypsin-like activity. Both Flag–PAC1 and Flag–PAC2 effectively co-precipitated with subunits from fraction 10 (Supplementary Fig. 1b, d). Moreover, even in fraction 16, which contained predominantly mature 20S proteasomes, they precipitated mainly with pro-β1i (Supplementary Fig. 1d), confirming that PAC1 and PAC2 associate specifically with precursor 20S proteasomes. Notably, the concentrations of precursor proteasomes were increased in both transfected cell lines (Supplementary Fig. 1c).

To examine the behaviour of endogenous PAC1 and PAC2 in detail, extracts from HEK293T cells were separated by lower density (4–24%) glycerol gradient centrifugation to resolve the precursor complexes. PAC1 and PAC2 were distributed mostly in the precursor fractions (Fig. 1a). Notably, the peaks of PAC1 and PAC2 were located in a fraction (fraction 12) lighter than that of the half-proteasomes (fraction 16), which contained hUmp1 and pro-β2. Moreover, the peaks of α5–α7 in precursor fractions were also located in fraction 12. Treatment with MG132 resulted in an accumulation of PAC1 and PAC2 in 20S proteasome fractions (Fig. 1a, right). The association of PAC1 and PAC2 with proteasomes was observed in fractions 12, 16 and 22 (Fig. 1b). When cells were treated with MG132, greater amounts of PAC1 and PAC2 were precipitated from fraction 22. Neither α4 nor α6 was associated with pro-β2 or hUmp1 in fraction 12. These results indicate that PAC1 and PAC2 form a complex with precursor 20S proteasomes before hUmp1 and the pro-β subunits are recruited, and suggest that PAC1 and PAC2 are chaperones for the maturation of 20S proteasomes and are released from or degraded by the newly assembled 20S proteasomes, analogous to the role of Ump1 in yeast[14].

To determine the composition of the peak of α-subunits that contained PAC1 and PAC2, fractions 12 and 16 were immunoprecipitated with antibodies against α6 and separated by two-dimensional polyacrylamide gel electrophoresis (2D-PAGE). Fraction 12 contained all seven α-subunits but no β-subunits, some of which were apparently detected in fraction 16 (Fig. 1c). Immunoblot analysis confirmed that all α-subunits except α1, which was difficult to distinguish by immunoblotting, were present in fraction 12 (Fig. 1d). The size of this complex (Fig. 1a), coupled with the absence of pro-β subunits or hUmp1 (Fig. 1a–c), means that it is

[1]Laboratory of Frontier Science, Core Technology and Research Center, Tokyo Metropolitan Institute of Medical Science, Bunkyo-ku, Tokyo 113-8613, Japan. [2]Institute of Molecular Biology and Physiology, University of Copenhagen, 13 Universitetsparken, DK 2100 Copenhagen, Denmark. [3]National Institute of Advanced Industrial Science and Technology, Biological Information Research Center, Kohtoh-ku, Tokyo 135-0064, Japan. [4]PRESTO, Japan Science and Technology Agency, Kawaguchi, Saitama 332-0012, Japan.

most probably a ring of all seven α-subunits, namely an α-ring. Immunoprecipitation in lower salt conditions showed that PAC1 and PAC2 are near-stoichiometric components of α-rings and that the association of PAC1 and PAC2 with α-subunits is salt labile (Fig. 1e, f). PAC1 was detected at a wide range of isoelectic point (pI) values, suggesting that it undergoes posttranslational modification (Fig. 1f). These results suggest that the PAC1–PAC2 complex and hUmp1 are distinct entities that work at different points in 20S proteasome assembly, and that PAC1 and PAC2 function as chaperone-like molecules at an earlier stage of 20S proteasome assembly relative to hUmp1.

Next, we characterized the interaction between PAC1 and PAC2. Coexpression of PAC1 and PAC2 in *Escherichia coli* and *in vitro* cotranscription–translation (IVTT) indicated that the two proteins bind directly (Supplementary Fig. 2a, b). Furthermore, PAC1 tagged with glutathione *S*-transferase (GST) pulled down PAC2 tagged with haemagglutinin A (HA) but not HA–PAC1, whereas GST–PAC2 pulled down HA–PAC1 but not HA–PAC2 *in vitro* (Supplementary Fig. 2b), indicating that PAC1 and PAC2 form hetero-oligomers but not homo-oligomers. No direct interaction between the PAC complex and hUmp1 was detected (Supplementary Fig. 2c). To determine the stoichiometry of the PAC complex, we coexpressed 3× Flag–PAC1 and 6× His–PAC2 in *E. coli* and purified the complex. PAC1 and PAC2 formed a complex at 1:1 stoichiometry with a relative molecular mass ($M_r$) corresponding to bovine serum albumin (67,000; Fig. 2a, b), indicating that the complex is a heterodimer.

To clarify further the nature of the PAC complex, we examined the half-lives of PAC1 and PAC2 by pulse-chase experiments. Both PAC1 and PAC2 turned over rapidly with similar half-lives of about 40 min (Fig. 2c). Treating the cells with MG132 markedly prolonged their half-lives, indicating that the PAC heterodimer is degraded by proteasomes. Because assembly of 20S proteasomes is complete within 1 h (ref. 21), the half-life of the PAC complex is consistent with the complex functioning as a chaperone for proteasome assembly and with its degradation on the completion of 20S proteasomes assembly.

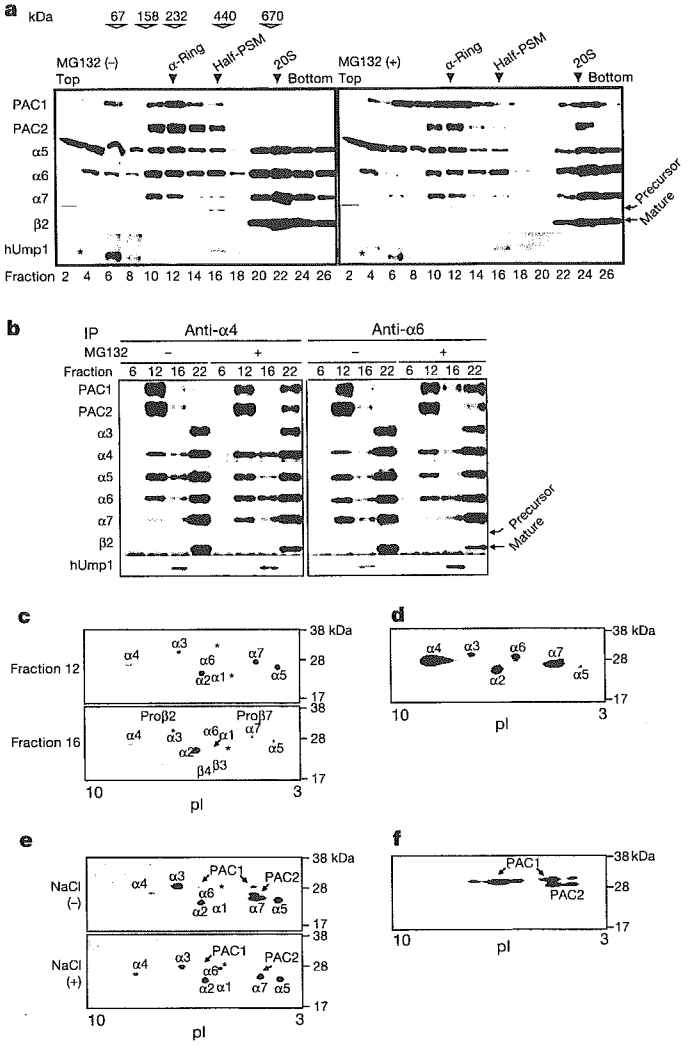


**Figure 1 | PAC1 and PAC2 associate with precursor proteasomes.** **a**, Glycerol gradient centrifugation (4–24%) of HEK293T cell extracts untreated or treated with MG132. Fractions were immunoblotted for the indicated proteins. Size markers and subcomplexes of proteasomes are indicated by open and filled arrowheads, respectively. Half-PSM indicates half-proteasomes. Asterisks indicate nonspecific bands. **b**, Fractions from **a** were immunoprecipitated with antibody against α4 or α6 and then subjected to immunoblotting. **c–f**, Fractions 12 (**c–f**) and 16 (**c**) from **a** were immunoprecipitated with beads conjugated to antibody against α6, washed with buffer A containing 150 mM (**c**, **d**), 0 mM or 50 mM (**e**, **f**) NaCl, eluted with glycine-HCl, and resolved by 2D-PAGE with silver (**c**) or Coomassie blue (**e**) staining. Asterisks denote unidentified spots. The top gel in **c** was immunoblotted with MCP231 and MCP34 antibodies against α-subunits and α4, respectively (**d**). The top gel in **e** was immunoblotted with antibodies against PAC1 and PAC2 (**f**). The non-uniformity of the spot intensity (**c**, **e**) may be due to a staining artefact because even in the half-proteasome fraction (fraction 16), which should contain all α-subunits in equal amounts, the spot intensities of α-subunits varied, resembling the pattern of fraction 12.

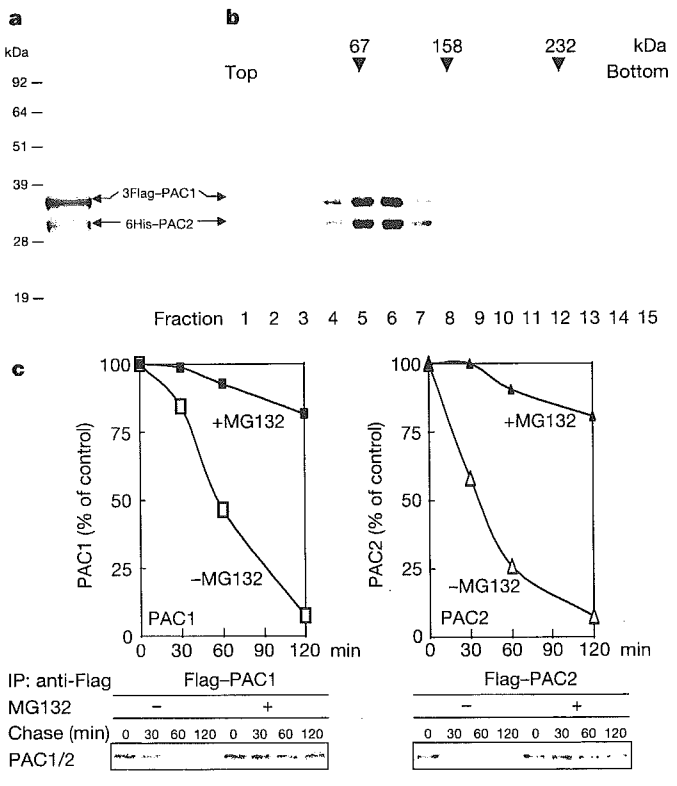


**Figure 2 | The PAC1-PAC2 heterodimer is rapidly degraded by proteasomes.** **a**, Coomassie blue staining of a copurified complex of 3× Flag–PAC1 and 6× His–PAC2 expressed in bacterial cells. **b**, The purified PAC complex in **a** was separated by 4–17% glycerol gradient centrifugation and subjected to SDS–PAGE with Coomassie staining. Arrowheads indicate size markers. **c**, Half-lives of PAC1 and PAC2. HeLa cells stably transfected with Flag–PAC1 or Flag–PAC2 were radiolabelled and chased in the presence or absence of MG132. Bottom panels show autoradiography; top panels show quantitative analysis of the bands.

To clarify the role of PAC1 and PAC2 in the assembly of the 20S proteasome *in vivo*, we used short interfering RNA (siRNA) to knock down the expression of PAC1 and PAC2. Knockdown of PAC1 resulted in loss of both PAC1 and PAC2 protein. Knockdown of PAC2 was also associated with a decrease in PAC1 protein (Fig. 3a), indicating that PAC1 and PAC2 are stable only when they form a heterodimer. Both PAC1- and PAC2-knockdown cells showed reduced proteolytic activity, as indicated by an assay of the antizyme-dependent degradation of ornithine decarboxylase (Supplementary Fig. 3a). Consequently, PAC-knockdown cells accumulated polyubiquitin-conjugated proteins, were sensitive to stress such as $Cd^{2+}$, and showed slow growth (Supplementary Fig. 3b–d).

We subjected the PAC-knockdown cells, as well as control and hUmp1-knockdown cells, to 4–24% glycerol gradient analysis. Notably, α-rings were hardly detected in either the PAC1- or the PAC2-knockdown cells (Fig. 3b). Instead, the α-subunits accumulated in fractions corresponding to half-proteasomes. This accumulation was not accompanied by an increase in pro-β2, pro-β5 or hUmp1, however, suggesting that the half-proteasomes were not normal. To confirm this notion, fraction 16 from the knockdown cells was immunoprecipitated with antibody against α6. Even though nearly equal amounts of α-subunits were loaded in the different samples, pro-β2, pro-β5 and hUmp1 were detected in much smaller amounts in PAC-knockdown cells (Fig. 3c), indicating that fraction 16 in PAC-knockdown cells contained mostly abnormally assembled α-subunits. This abnormal complex did not contain Rpt subunits, the components of 19S regulatory particles (Supplementary Fig. 3e, f), precluding the possibility that the mobility shift of α-subunits in PAC-knockdown cells was due to the premature association of α-subunits with Rpt subunits. On the basis of their sizes, these complexes are probably dimers of α-rings.

In hUmp1-knockdown cells, by contrast, we observed a marked reduction in 20S proteasomes but apparently normal α-rings and half-proteasomes, demonstrating the crucial role of hUmp1 in the dimerization of half-proteasomes. There was a strong increase in the free forms of some α-subunits in hUmp1-knockdown cells and a moderate increase in PAC-knockdown cells (Supplementary Fig. 3g). Assays of peptidase activities showed a significant reduction in activity of both the 20S and the 26S proteasome fractions in PAC-knockdown cells, although the effect of hUmp1 knockdown was more intense (Supplementary Fig. 3h). These data show definitively that the PAC complex has a pivotal role in the assembly of 20S proteasomes, specifically in keeping α-rings competent for the subsequent formation of half-proteasomes.

To elucidate the mechanism of PAC complex function, we tested the direct association of the complex with all of the subunits of 20S proteasomes. The PAC complex specifically interacted with α5 and α7, but not with other α-subunits or with any of the β-subunits *in vitro* (Supplementary Fig. 4a). Because Fig. 1a shows that the PAC1–PAC2 complex is found not only in α-ring fractions but also in lighter fractions, we considered whether it is involved in α-ring assembly. Immunoprecipitation with an antibody against Flag after the coexpression of all seven α-subunits, of which α5 was Flag-tagged, by IVTT showed that all α-subunits co-precipitated with Flag–α5 in larger amounts in the presence of the PAC complex than in its absence (Supplementary Fig. 4b). Immunoprecipitation with anti-Flag antibody after the coexpression of Flag–PAC1, PAC2 and α-subunits showed that PAC1 precipitated not only α5 and α7 but also all of the other α-subunits (Supplementary Fig. 4c), implying that it has a role in attracting α-subunits to each other.

We examined these interactions under more physiological conditions. Extracts of 293T cells that stably express Flag–PAC1 were separated by 4–24% glycerol gradient, and fractions corresponding to early α-subunit assembly intermediates and α-rings (fractions 8 and 12 in Fig. 1a, respectively) were immunoprecipitated with anti-Flag antibody and subjected to 2D-PAGE. PAC1 in fraction 12 co-precipitated all seven α-subunits, whereas PAC1 in fraction 8 co-precipitated several unidentified spots other than α-subunits, which made it difficult to identify α-subunits except for α5 and α7 by Coomassie staining (Fig. 4a, left). Immunoblot analysis showed that all α-subunits were present in the α-ring fraction, although α1 was difficult to distinguish (Fig. 4a, right), consistent with the findings in Fig. 1c. In contrast, PAC1 in fraction 8 co-precipitated a restricted set

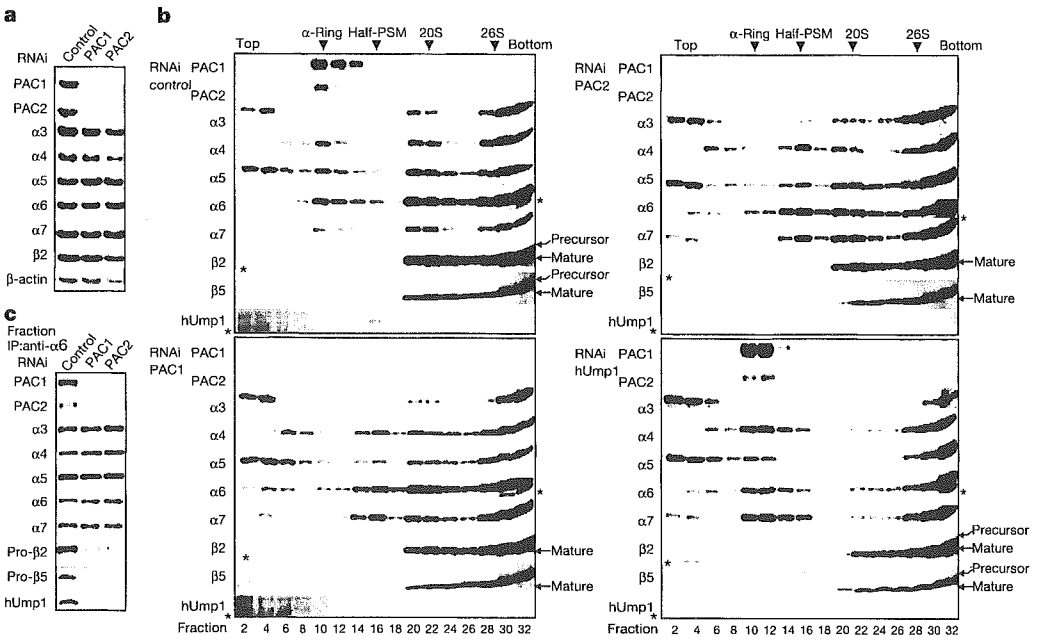


**Figure 3 | siRNA-mediated knockdown of PAC1 and PAC2 impairs proteasome assembly. a–c**, siRNA targeting PAC1 or PAC2, or control siRNA, was transfected into HEK293T cells. Knockdown of hUmp1 was also analysed in **b**. Whole-cell extracts (**a**), fractions separated by 4–24% glycerol gradient centrifugation (**b**), and immunoprecipitates obtained from fraction 16 in **b** with antibodies against α6 (**c**) were immunoblotted for the indicated proteins. Asterisks indicate nonspecific bands.

of α-subunits in which α3 and α4 were hardly detected. These results indicate that there is a hierarchy among α-subunits in their incorporation into α-rings, and that the PAC complex associates with the α-subunits before α-rings are complete, and functions as a scaffold for α-ring assembly.

Finally, we tested whether the complex of α-subunits in fraction 12 is a unique species. The affinity-purified complex from fraction 12 was subjected to native-PAGE. We found that the complex had a unique electrophoretic mobility (Fig. 4b). Moreover, the complex was eluted with a single sharp peak by anion-exchange chromatography (Fig. 4c). Thus, this complex is a unique species biochemically and is a genuine α-ring rather than a group of heterogeneous and incomplete α-ring precursors.

Our present work provides a model in which the chaperone complex PAC1–PAC2 mediates the formation of α-rings, keeps the rings competent for half-proteasome formation, and is required for proper proteasome maturation and cellular integrity (Fig. 4d). (See Supplementary Discussion for a more detailed description.)

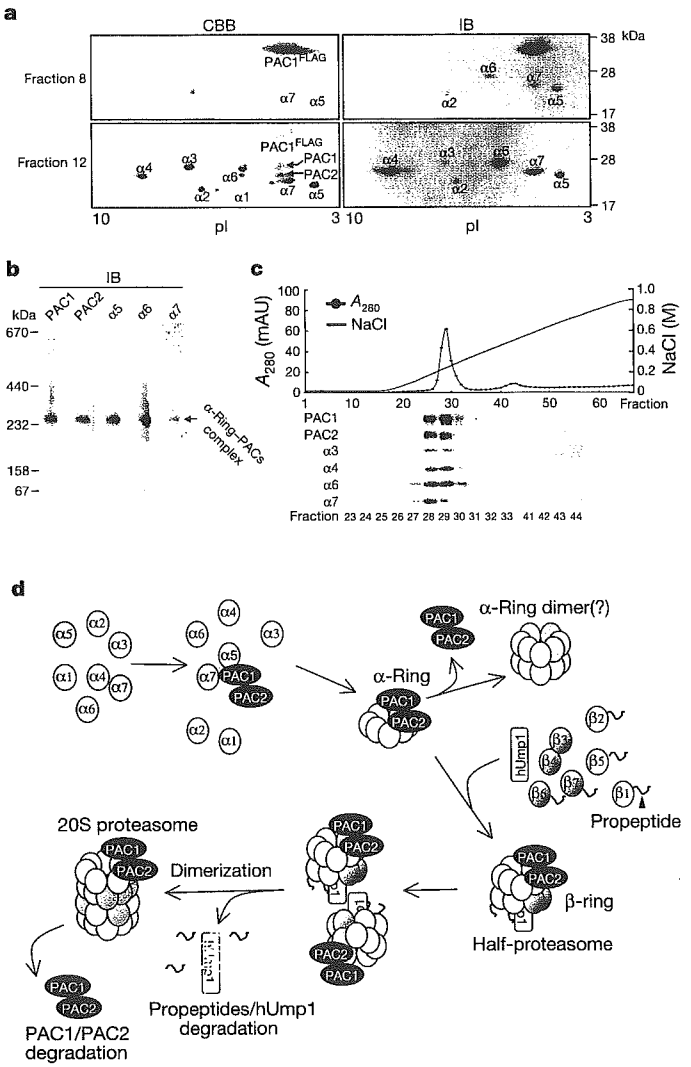


**Figure 4 | PAC1–PAC2 provides a scaffold for α-ring formation. a**, Extracts of HEK293T cells transfected with Flag–PAC1 were fractionated as in Fig. 1a. The Flag–PAC1 complexes from fractions 8 and 12 were purified with M2 agarose, resolved by 2D-PAGE and detected by Coomassie blue staining (left) or immunoblotting as in Fig. 1d (right). Asterisks denote unidentified spots. **b, c**, Purified Flag–PAC1 complex from fraction 12 was subjected to native-PAGE (**b**) or anion-exchange chromatography (**c**), followed by immunoblotting. **d**, Multistep model of the ordered assembly of mammalian 20S proteasomes. Some of the newly synthesized free α-subunits bind to the PAC1–PAC2 heterodimer, which provides a scaffold for α-ring formation, thereby suppressing the off-pathway aggregation of α-subunits and keeping α-rings competent for half-proteasome formation. Two half-proteasomes then dimerize, the β-subunits are processed and hUmp1 is degraded. The PAC1–PAC2 complex is subsequently degraded by the newly formed active 20S proteasomes.

## METHODS

See Supplementary Methods for procedures used in the experiments in Supplementary Figs 1–4.

**DNA constructs and cell culture.** We synthesized cDNAs encoding PAC1, PAC2, hUmp1 and proteasome α- and β-subunits from total RNA isolated from HeLa cells using Superscript II (Invitrogen). PCR was carried out on the cDNA with Pyrobest DNA polymerase (Takara). All of the amplified fragments were cloned into pcDNA3.1 (Invitrogen) and sequenced for confirmation. For expression of GST fusion proteins, the cDNAs were subcloned into pGEX6P-1 (Amersham). Transfections of 293T cells were done with Fugene 6 (Roche). Stable transfections of HeLa cells or 293T cells were done with Lipofectamine 2000 (Invitrogen), and the cells were selected with 1 mg ml$^{-1}$ of G418 or 5 μg ml$^{-1}$ of puromycin, respectively. We used 20 μM MG132 (Peptide Institute) to inhibit proteasome activities 2 h before the cells were collected.

**Protein extracts, immunological analysis and antibodies.** Cells were lysed in ice-cold buffer A containing 50 mM Tris-HCl (pH 7.5), 0.5% (v/v) Nonidet P40, 1 mM dithiothreitol (DTT) and 2 mM ATP, and the extracts were clarified by centrifugation at 20,000*g* for 10 min at 4 °C. SDS–PAGE (12% gel or 4–12% gradient Bis-Tris gel; Invitrogen) and native-PAGE (3–8% gradient Tris-acetate gel; Invitrogen) were done in accordance with the manufacturer's instructions. The separated proteins were transferred onto polyvinylidene difluoride membrane and reacted with the indicated antibody. Development was done with Western Lighting reagent (Perkin Elmer). Polyclonal antibodies against hUmp1, PAC1 and PAC2 were raised in rabbits using a synthetic peptide ($E_{115}$DILNDPSQSE$_{125}$), and recombinant PAC1 and PAC2 protein, respectively. PAC1 and PAC2 were produced and purified as GST fusion proteins, and GST was removed by PreScission protease (Amersham).

Antibodies against proteasome α3 subunit (MCP257), α4 (MCP34), α5 (MCP196), α6 (MCP20), α7 (MCP72), β2 (MCP168) and α-subunits (MCP231, which reacts with all α-subunits except α4) were purchased from BioMol. Antibodies against β5 (P93250), β6 (P93199) and β1i were prepared as described[22]. We used antibodies against the Flag tag (Sigma) and β-actin (Chemicon), and horseradish peroxidase (HRP)-conjugated rabbit anti-mouse and goat anti-rabbit IgG (Jackson ImmunoResearch) for immunodetection. For immunoprecipitation of the Flag epitope, we used M2 agarose (Sigma). For immunoprecipitation of proteasomes, we used antibody MCP34 or MCP20 bound to protein G Sepharose (Amersham). In the experiments in Fig. 1c–f, we used MCP20 crosslinked to NHS-activated Sepharose (Amersham). These beads were added to the extracts, mixed under constant rotation for 2 h at 4 °C, washed four times with buffer A (except in the experiments in Fig. 1c–f), and boiled in SDS sample buffer, or eluted with 100 μg ml$^{-1}$ of Flag peptides (Sigma) or with 0.2 M glycine-HCl (pH 2.8). Densitometric analysis was done with Image Gauge software (Fujifilm). 2D-PAGE was done as described[23].

**Glycerol gradient analysis.** Samples and molecular weight markers (Amersham) were fractionated by 4–17% (v/v), 4–24% (v/v) or 8–32% (v/v) linear glycerol density gradient centrifugation (22 h, 100,000*g*) as described[22].

**Purification of PAC1–PAC2 complex.** We coexpressed 3× FLAG–PAC1 and 6× His–PAC2 in *E. coli* using a pRSFDuet-1 vector (Novagen). The cell pellets were lysed in buffer B containing 20 mM sodium phosphate (pH 7.8), 500 mM NaCl and 1.0% Triton X-100, and sonicated. Ni-NTA Sepharose (Qiagen) was added to the extracts, which were then washed with buffer C containing 20 mM sodium phosphate (pH 6.0) and 500 mM NaCl, and eluted with buffer C plus 100 mM imidazole. The eluted products were further purified with M2 agarose and eluted with 100 μg ml$^{-1}$ of Flag peptide (Sigma).

**Pulse-chase experiments.** Cells were incubated with methionine-free medium for 1 h, metabolically labelled with $^{35}$S-methionine for 1 h, and then washed and chased for the indicated time. The cell lysates were immunoprecipitated with M2 agarose, fractionated by SDS–PAGE and visualized by autoradiography.

**RNAi experiments.** siRNAs targeting human PAC1, PAC2 and hUmp1 with the following 19-nucleotide sequences were designed by B-Bridge and synthesized by Dharmacon: PAC1, 5′-CCAGAAGCUUGAAGGGUUU-3′; PAC2, 5′-GCAUAAAUGCUGAAGUGUA-3′; hUmp1, a mixture of 5′-GCAAGUGG ACCUUUUGAAA-3′ and 5′-CCUGAGAAUUUCUGCUCAA-3′. Control siRNA (Non-specific Control Duplex VIII) was purchased from B-Bridge. Transfections of siRNAs into HEK293T cells were done with Lipofectamine

2000 at a final concentration of 50 nM in six-well dishes. The cells were analysed 72 h after transfection.

**Assay of proteasome activity.** Peptidase activity was measured by using a fluorescent peptide substrate, succinyl-Leu-Leu-Val-Tyr-7-amido-4-methylcoumarin (Suc-LLVY-MCA), as described[23].

**Chromatography.** Anion-exchange chromatography was done with a Resource Q column (Amersham). Bound proteins were eluted with a salt gradient of 0–1 M NaCl in a buffer containing 50 mM Tris-HCl (pH 8.0), 1 mM DTT and 5% glycerol.

**Received 27 June; accepted 2 August 2005.**


1. Pickart, C. M. Mechanisms underlying ubiquitination. *Annu. Rev. Biochem.* **70**, 503–533 (2001).
2. Glickman, M. H. & Ciechanover, A. The ubiquitin–proteasome proteolytic pathway: destruction for the sake of construction. *Physiol. Rev.* **82**, 373–428 (2002).
3. Baumeister, W., Walz, J., Zuhl, F. & Seemuller, E. The proteasome: paradigm of a self-compartmentalizing protease. *Cell* **92**, 367–380 (1998).
4. Groll, M. *et al.* Structure of 20S proteasome from yeast at 2.4 Å resolution. *Nature* **386**, 463–471 (1997).
5. Unno, M. *et al.* The structure of the mammalian 20S proteasome at 2.75 Å resolution. *Structure (Camb.)* **10**, 609–618 (2002).
6. Zwickl, P., Kleinz, J. & Baumeister, W. Critical elements in proteasome assembly. *Nat. Struct. Biol.* **1**, 765–770 (1994).
7. Gerards, W. L. *et al.* The human α-type proteasomal subunit HsC8 forms a double ringlike structure, but does not assemble into proteasome-like particles with the β-type subunits HsDelta or HsBPROS26. *J. Biol. Chem.* **272**, 10080–10086 (1997).
8. Yao, Y. *et al.* α5 subunit in *Trypanosoma brucei* proteasome can self-assemble to form a cylinder of four stacked heptamer rings. *Biochem. J.* **344**, 349–358 (1999).
9. Yang, Y., Fruh, K., Ahn, K. & Peterson, P. A. *In vivo* assembly of the proteasomal complexes, implications for antigen processing. *J. Biol. Chem.* **270**, 27687–27694 (1995).
10. Chen, P. & Hochstrasser, M. Autocatalytic subunit processing couples active site formation in the 20S proteasome to completion of assembly. *Cell* **86**, 961–972 (1996).
11. Schmidtke, G. *et al.* Analysis of mammalian 20S proteasome biogenesis: the maturation of β-subunits is an ordered two-step mechanism involving autocatalysis. *EMBO J.* **15**, 6887–6898 (1996).
12. Nandi, D., Woodward, E., Ginsburg, D. B. & Monaco, J. J. Intermediates in the formation of mouse 20S proteasomes: implications for the assembly of precursor β subunits. *EMBO J.* **16**, 5363–5375 (1997).
13. Schmidtke, G., Schmidt, M. & Kloetzel, P. M. Maturation of mammalian 20 S proteasome: purification and characterization of 13 S and 16 S proteasome precursor complexes. *J. Mol. Biol.* **268**, 95–106 (1997).
14. Ramos, P. C., Hockendorff, J., Johnson, E. S., Varshavsky, A. & Dohmen, R. J. Ump1p is required for proper maturation of the 20S proteasome and becomes its substrate upon completion of the assembly. *Cell* **92**, 489–499 (1998).
15. Griffin, T. A., Slack, J. P., McCluskey, T. S., Monaco, J. J. & Colbert, R. A. Identification of proteassemblin, a mammalian homologue of the yeast protein, Ump1p, that is required for normal proteasome assembly. *Mol. Cell. Biol. Res. Commun.* **3**, 212–217 (2000).
16. Witt, E. *et al.* Characterisation of the newly identified human Ump1 homologue POMP and analysis of LMP7(β5i) incorporation into 20 S proteasomes. *J. Mol. Biol.* **301**, 1–9 (2000).
17. Burri, L. *et al.* Identification and characterization of a mammalian protein interacting with 20S proteasome precursors. *Proc. Natl Acad. Sci. USA* **97**, 10348–10353 (2000).
18. Natsume, T. *et al.* A direct nanoflow liquid chromatography-tandem mass spectrometry system for interaction proteomics. *Anal. Chem.* **74**, 4725–4733 (2002).
19. Vidal-Taboada, J. M. *et al.* Down syndrome critical region gene 2: expression during mouse development and in human cell lines indicates a function related to cell proliferation. *Biochem. Biophys. Res. Commun.* **272**, 156–163 (2000).
20. Bahar, R. *et al.* Growth retardation, polyploidy, and multinucleation induced by Clast3, a novel cell cycle-regulated protein. *J. Biol. Chem.* **277**, 40012–40019 (2002).
21. Ahn, K. *et al. In vivo* characterization of the proteasome regulator PA28. *J. Biol. Chem.* **271**, 18237–18242 (1996).
22. Tanahashi, N. *et al.* Hybrid proteasomes. Induction by interferon-γ and contribution to ATP-dependent proteolysis. *J. Biol. Chem.* **275**, 14336–14445 (2000).
23. Murata, S. *et al.* Immunoproteasome assembly and antigen presentation in mice lacking both PA28α and PA28β. *EMBO J.* **20**, 5898–5907 (2001).


**Supplementary Information** is linked to the online version of the paper at www.nature.com/nature.

**Acknowledgements** We thank Y. Murakami for the ornithine decarboxylase degradation assay system, K. Furuyama for technical support, and D. Finley for comments on the manuscript. This work was supported by grants from the Japanese Science and Technology Agency (to S.M.), the Ministry of Education, Science and Culture of Japan (to S.M. and K.T.) and the New Energy and Industrial Technology Development Organization (to T.N.). Y.H. was supported by the Japanese Society for the Promotion of Science.

**Author Information** The sequences for human PAC1 and PAC2 have been deposited in GenBank under accession numbers BR000236 and BR000237, respectively. Reprints and permissions information is available at npg.nature.com/reprintsandpermissions. The authors declare no competing financial interests. Correspondence and requests for materials should be addressed to S.M. (smurata@rinshoken.or.jp) or K.T. (tanakak@rinshoken.or.jp).

nature
structural &
molecular biology

# Structural basis of sugar-recognizing ubiquitin ligase

Tsunehiro Mizushima[1,2], Takeshi Hirao[3], Yukiko Yoshida[2,4], Soo Jae Lee[5], Tomoki Chiba[2], Kazuhiro Iwai[4,6], Yoshiki Yamaguchi[3,4], Koichi Kato[3,4,7], Tomitake Tsukihara[5] & Keiji Tanaka[2]

**$SCF^{Fbs1}$ is a ubiquitin ligase that functions in the endoplasmic reticulum (ER)-associated degradation pathway. Fbs1/Fbx2, a member of the F-box proteins, recognizes high-mannose oligosaccharides. Efficient binding to an N-glycan requires di-*N*-acetylchitobiose (chitobiose). Here we report the crystal structures of the sugar-binding domain (SBD) of Fbs1 alone and in complex with chitobiose. The SBD is composed of a ten-stranded antiparallel β-sandwich. The structure of the SBD–chitobiose complex includes hydrogen bonds between Fbs1 and chitobiose and insertion of the methyl group of chitobiose into a small hydrophobic pocket of Fbs1. Moreover, NMR spectroscopy has demonstrated that the amino acid residues adjoining the chitobiose-binding site interact with the outer branches of the carbohydrate moiety. Considering that the innermost chitobiose moieties in N-glycans are usually involved in intramolecular interactions with the polypeptide moieties, we propose that Fbs1 interacts with the chitobiose in unfolded N-glycoprotein, pointing the protein moiety toward E2 for ubiquitination.**

So far, numerous studies have emphasized the physiological importance of the ubiquitin- and proteasome-mediated proteolytic pathway[1]. The ubiquitination reaction is catalyzed by an elaborate cascade system, consisting of activating (E1), conjugating (E2) and ligating (E3) enzymes[1,2]. Of these enzymes, E3 enzymes are considered to exist as molecules with a large diversity and to have a principal role in the selection of target proteins for ubiquitination in a temporally and spatially regulated fashion[3].

One of the best-characterized E3 enzymes is the SCF complex (composed of Skp1, Cul1, Roc1 (also called Rbx1) and an F-box protein), which regulates degradation of a broad range of cellular proteins[4]. The F-box proteins consist of an F-box domain that binds to Skp1, and various C-terminal substrate recognition regions, which are subclassified into a family of proteins named Fbw and Fbl that contain WD40-repeat and leucine-rich repeat (LRR) domains, respectively[5]. In addition, the remaining groups have been provisionally classified as Fbx proteins, which show no homology to any other known proteins[5]. However, we recently discovered a third category of the F-box protein family named Fbs (F-box sugar recognition)/FBG[6], consisting of at least five structurally related proteins including Fbs1 (named originally as Fbx2)[7] and Fbs2/Fbx6b (ref. 8). Fbw and Fbl proteins usually recognize the phosphorylation status of the substrate, and the tertiary structures of some of these proteins, such as Fbw1/βTrCP, Fbw7/Cdc4 and Fbl1/Skp2, have been determined by X-ray crystallography, providing valuable information for determining the molecular recognition mechanisms of target proteins[9–12]. However, the molecular basis underlying the ability of Fbs proteins to recognize target glycoproteins remains to be clarified.

Eukaryotic cells have an abundant and diverse repertoire of N-linked oligosaccharide structures, but the role of N-glycosylation of the proteins remains largely unknown. N-glycans have recently been shown to have an important role in glycoprotein transport and sorting[13,14]. N-glycoproteins are also subjected to 'quality control,' in which aberrant proteins are distinguished from properly folded proteins and retained in the ER[15]. When the improperly folded or incompletely assembled proteins fail to restore their functional states, they are degraded by the ER-associated degradation (ERAD) system, which involves retrograde transfer of proteins from the ER to the cytosol and subsequent degradation mediated by ubiquitin and proteasomes[16]. Recently, we identified the $SCF^{Fbs1}$ as an E3 ubiquitin–ligase complex that ubiquitinates N-linked glycoproteins, serving to clear these glycoproteins in the cytosol of the cell[7]. Fbs1 recognizes N-linked high-mannose oligosaccharides, especially the internal diacetylchitobiose structure[8]. However, the molecular mechanism of the recognition of N-glycans by Fbs1 is unknown at present. To understand the molecular basis of the interaction between Fbs1 and N-glycans, we conducted crystal structural analyses of the SBD of Fbs1 and its complex with chitobiose.

## RESULTS

### Overall structure of the SBD in Fbs1

The structure of the SBD of Fbs1, as determined at a resolution of 2.0 Å (Table 1), is an ellipsoid composed of a ten-stranded antiparallel β-sandwich with two α-helices (Fig. 1a,b). This structure is

[1]Precursory Research for Embryonic Science and Technology (PRESTO), Japan Science and Technology Agency, Kawaguchi, Saitama 332-0012, Japan. [2]Tokyo Metropolitan Institute of Medical Science, Bunkyo-ku, Tokyo 113-8613, Japan. [3]Department of Structural Biology and Biomolecular Engineering, Graduate School of Pharmaceutical Sciences, Nagoya City University, 3-1 Tanabe-dori, Mizuho-ku, Nagoya 467-8603, Japan. [4]Core Research for Evolutional Science and Technology (CREST), Japan Science and Technology Agency, Saitama 332-0012, Japan. [5]Institute for Protein Research, Osaka University, 3-2 Yamadaoka, Suita, Osaka 565-0871, Japan. [6]Department of Molecular Cell Biology, Graduate School of Medicine, Osaka City University, Osaka 545-8585, Japan. [7]Genomic Sciences Center, RIKEN Yokohama Institute, 1-7-29 Suehiro-cho, Tsurumi-ku, Yokohama 230-0045, Japan. Correspondence should be addressed to K.T. (tanakak@rinshoken.or.jp).

Published online 29 February 2004; doi:10.1038/nsmb732

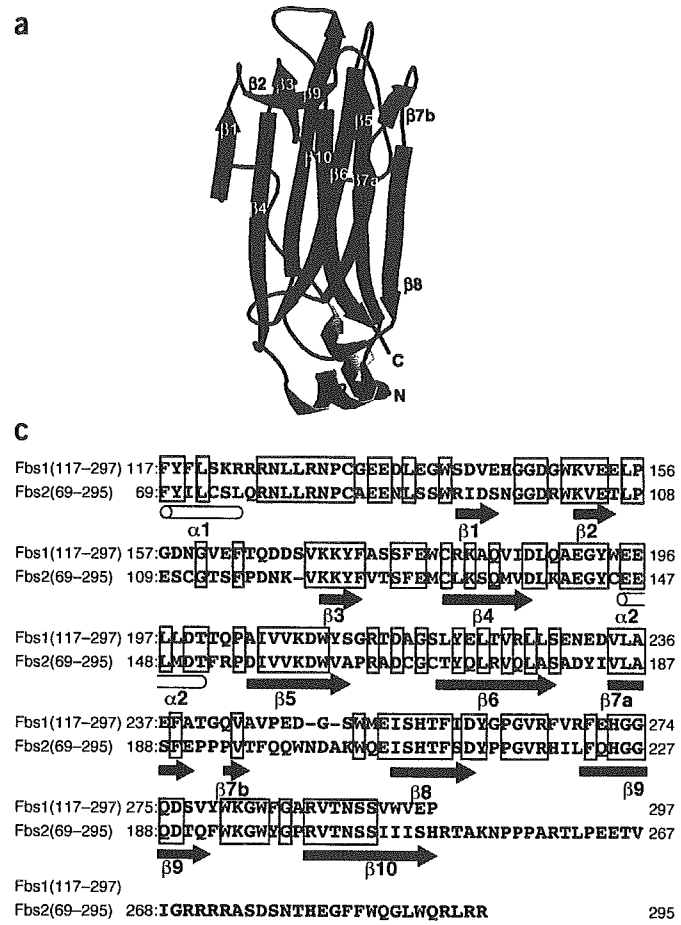


**Figure 1** Tertiary structure of SBD in Fbs1. (**a**) Overall structure of SBD of Fbs1 shown as a ribbon diagram. β-strands belonging to S1 and S2 are blue and red, respectively. Loops and helices are black and yellow, respectively. (**b**) A topology diagram of SBD. The α-helices are yellow cylinders labeled α1 and α2. The β-strands are arrows labeled β1–β10. The left and right forms of β-strands correspond to S1 and S2, respectively, as in **a**. N and C, N and C termini, respectively. (**c**) Amino acid sequences of SBD in Fbs1 and corresponding region of Fbs2. Amino acid residues are numbered in the N-to-C direction, for example, from position 117 to position 297 (C-terminal end) of Fbs1, and from 69 to 295 (C-terminal end) of Fbs2. Identical residues are boxed. Secondary structure elements are colored as **a**. Substrate-binding residues are red characters.

completely different from the folds of substrate-binding regions of F-box domains so far reported, including the WD40-repeat domain of CDC4 (ref. 11) and the LRR domain of Skp2 (ref. 12). Strands β1, β4, β6, β7 and β9 form one β-sheet, whereas the other β-sheet consists of strands β2, β3, β5, β8 and β10. These two sheets are named the S1 and S2 sheets, respectively (**Fig. 1a–c**). Strand β7, which is located at one edge of the S1 sheet, is composed of two segments (β7a and β7b) separated by a bent structure. The two α-helices (α1 and α2) lie at one end of the β-sandwich; the α1 helix is at the N terminus and α2 helix is in the loop between β4 and β5. Comparisons of the SBD structure described here with the Protein Data Bank using the Dali server[17] revealed that the SBD is structurally similar to certain lectins, such as the galectin-3 carbohydrate recognition domain[18] and second family 4 carbohydrate-binding modules of xylanase 10A (ref. 19), with r.m.s. deviation values of 2.8 and 2.8 Å, respectively. Indeed, both xylanase and galectin-3 domains are composed of 11-stranded antiparallel β-sandwiches, consisting of 5- and 6-stranded β-sheets, respectively, the overall structures of which resemble that of the SBD, although, in contrast to the SBD, they lack α-helices. Comparing their primary structures, the SBD shows considerable homology to the carbohydrate-binding domain of xylanase 10A, exhibiting amino acid identity of ~20%, whereas no obvious sequence homology was found between SBD and the carbohydrate recognition of galectin-3.

### The sugar-binding site

Next, we analyzed the structure of the SBD in complex with chitobiose. We could not obtain SBD crystals in the presence of chitobiose that diffracted to high resolution, so we introduced a C132A mutation in the SBD. The C132A SBD cocrystallized with chitobiose, and the structure of the C132A SBD–chitobiose complex was determined at 2.4 Å resolution (**Fig. 2a** and **Table 1**). The r.m.s. deviation values between SBD and the C132A mutant–chitobiose complex were 0.53 Å and 0.83 Å for the main chain and all atoms, respectively, indicating that the cysteine mutation hardly perturbs the conformation of the wild type SBD. It was also confirmed that this mutation did not alter the interaction and ubiquitination activities of glycoproteins (see **Fig. 3b**).

Chitobiose was clearly located in the difference electron density map (**Fig. 2a**), with *B*-factors as low as those of protein atoms around the chitobiose. The chitobiose in the SBD–chitobiose complex exhibited a *trans* conformation with respect to the *N*-acetyl groups, similar to the structures of a large number of N-glycan-binding proteins[20]. The bound chitobiose formed an intramolecular hydrogen bond between O6 of one GlcNAc(A) residue and O3 of the other GlcNAc(B) residue (**Fig. 2b,c**). The sugar-binding surface consists of two loops: L1 connects strands β3 and β4, and L2 is between strands β9 and β10. The GlcNAc(A) residue stacks on the aromatic ring of Trp280, as is often found in protein-carbohydrate interactions[21,22]. The GlcNAc-Trp280 stacking is stabilized by hydrogen bonds mediated by a water molecule between the O7 of the GlcNAc(A) and Nε1 of Trp280 (**Fig. 2c**), as well as a hydrogen bond between O6 of the GlcNAc(A) and the carbonyl oxygen atom of Lys281. The other GlcNAc(B) residue inserts the methyl group of its *N*-acetyl moiety into a small hydrophobic pocket surrounded by side chains of Phe177, Tyr279 and Lys281 (**Fig. 2a,b**) and forms a hydrogen bond between its hydroxyl and the main chain N atom of Lys281 (**Fig. 2c**). The orientation of the phenyl group of Tyr279 is stabilized by a hydrogen bond with the carboxyl group of Glu178. Upon N-glycoprotein uptake, the SBD swings the side chain of Lys281 (data not shown) and shields the methyl group from the molecular surface. The hydroxyl groups of the chitobiose almost exactly replace two binding site water molecules, which form a hydrogen bond to the backbone O and N of Lys281, respectively (**Fig. 2b,c**).

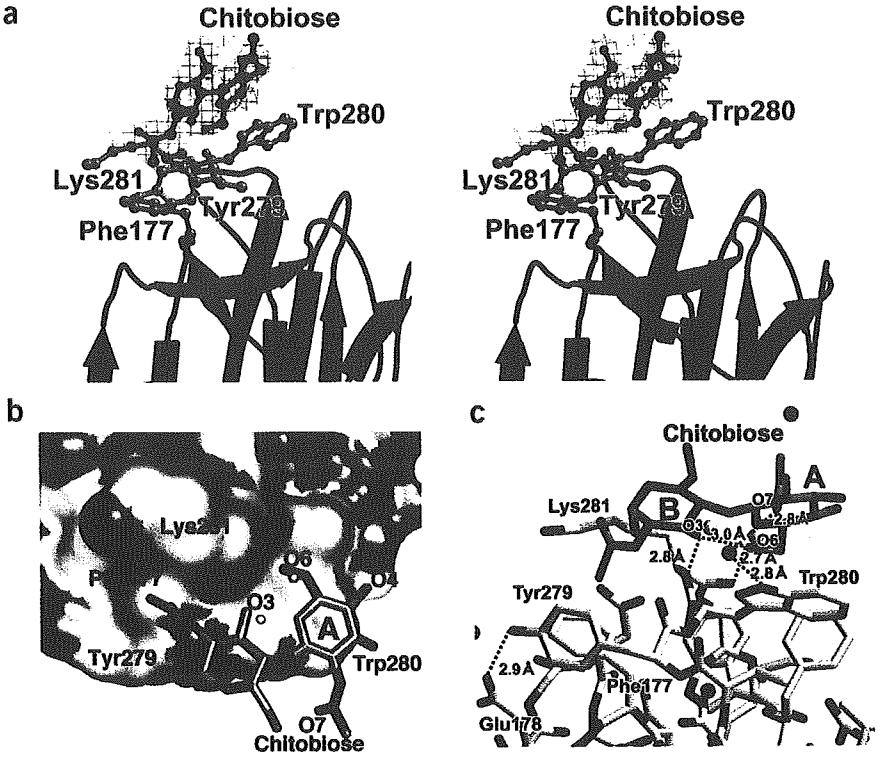


**Figure 2** Structure of SBD in complex with chitobiose. (**a**) Stereo view of the difference-density map ($F_o - F_c$ with phase from the Fbs1 model) of binding chitobiose, contoured at 2.1 σ, modeled into the electron density. β-strands belonging to S1 and S2 are blue and red, respectively. Loops are black. The bound chitobiose is orange, and the residues involved in the substrate binding (FYWK, see **Fig. 1c**) are green. (**b**) Molecular surface representation of the chitobiose-binding region. The bound chitobiose is shown in ball-and-stick representation. Two GlcNAc residues are represented by A and B. Cyan spheres are two water molecules of wild type SBD that are fixed on the molecular surface through hydrogen bonds with the backbone N and O of Lys281, respectively. These water molecules are replaced by O3 and O6 of the chitobiose upon formation of the SBD–chitobiose complex. (**c**) Stick representation of the amino acids involved in binding. Hydrogen bonds are dashed lines. Oxygen and nitrogen are red and blue, respectively. Symbols of two water molecules are as in **b**.

To verify that the crystal structure accurately represents the complex formed in solution, we introduced point mutations into the residues in the pocket, and examined the *in vitro* activities in binding the ribonuclease B (RNase B) carrying a high-mannose oligosaccharide (**Fig. 3a**). Indeed, F177A, Y279A and W280A mutations reduced binding to the RNase B, whereas the K281A mutation had no effect on the binding (**Fig. 3a**, left panel). We next tested the *in vivo* activities of these mutants in binding the precursor of integrin β1, one of the *in vivo* Fbs1 targets[7] that contains high-mannose oligosaccharides. Consistent with the *in vitro* results, F177A, Y279A and W280A, but not K281A, failed to bind integrin β1 (**Fig. 3a**, right panel). These results suggest that Phe177, Tyr279 and Trp280, located in the hydrophobic pocket at the edge of the β-sandwich, are important for interaction with chitobiose in the high-mannose oligosaccharides. In contrast, although comparison of the structure of the SBD alone and that of the SBD–chitobiose complex indicated that the side chain of Lys281 underwent a conformational change upon ligand binding, the *in vivo* and *in vitro* binding studies suggested that this conformational change was not essential for the recognition of oligosaccharides. Moreover, we examined the impact of these mutants on the ubiquitinating activities of the SCF onto GlcNAc-terminated fetuin (GTF) *in vitro* (**Fig. 3b**). SCF (Fbs1-W280A), which could not bind to N-glycans, failed to ubiquitinate GTF, whereas the ubiquitinating activities of the K281A mutant were retained. Taken together, these results indicate that the hydrophobic interactions between GlcNAc(A) residue and Trp280, and of GlcNAc(B) residue with the small hydrophobic pocket, are required for substrate recognition. In addition, the hydrogen bonds between the chitobiose and Fbs1 atoms (Nε1of Trp280 and the carbonyl oxygen atom of Lys281) are involved in selective binding to chitobiose.

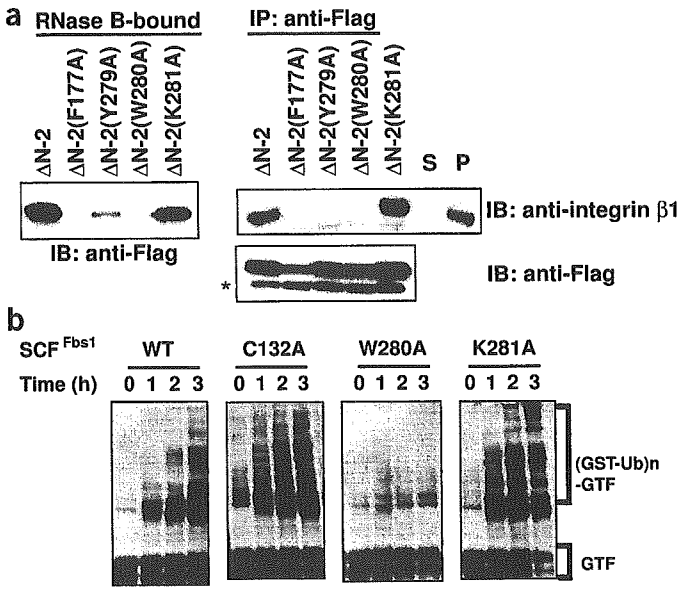


**Figure 3** Residues required for interaction of Fbs1 and glycoproteins with high-mannose oligosaccharides. (**a**) Neuro2a cells were transfected with Flag-tagged Fbs1 (ΔN-2) and its listed derivatives. In pull-down assay (RNase B-bound), each ΔN-2–expressing WCE was incubated with RNase B–immobilized beads; bound proteins were eluted by 0.1 M of chitobiose and then analyzed by immunoblotting with an antibody to Flag (anti-Flag). In immunoprecipitation with anti-Flag (IP: anti-Flag), the Fbs1-binding proteins in the immune complex were analyzed by immunoblotting using the anti-Flag or anti-integrin β1 antibody. Asterisks indicate the light chain of IgG. (**b**) *In vitro* ubiquitination of GTF by the $SCF^{Fbs1}$ E3–ligase system. The high-molecular-mass ubiquitinated GTF [(GST-Ub)n-GTF] was detected by immunoblotting with an antibody to fetuin.

### NMR analyses of the SBD-sugar interactions

We have previously reported that Fbs1 shows higher affinity to $Man_{3-9}GlcNAc_2$ glycans than to chitobiose, and the number of mannose residues did not influence the affinity[8]. We conducted NMR spectroscopic analysis to determine the contribution of the outer

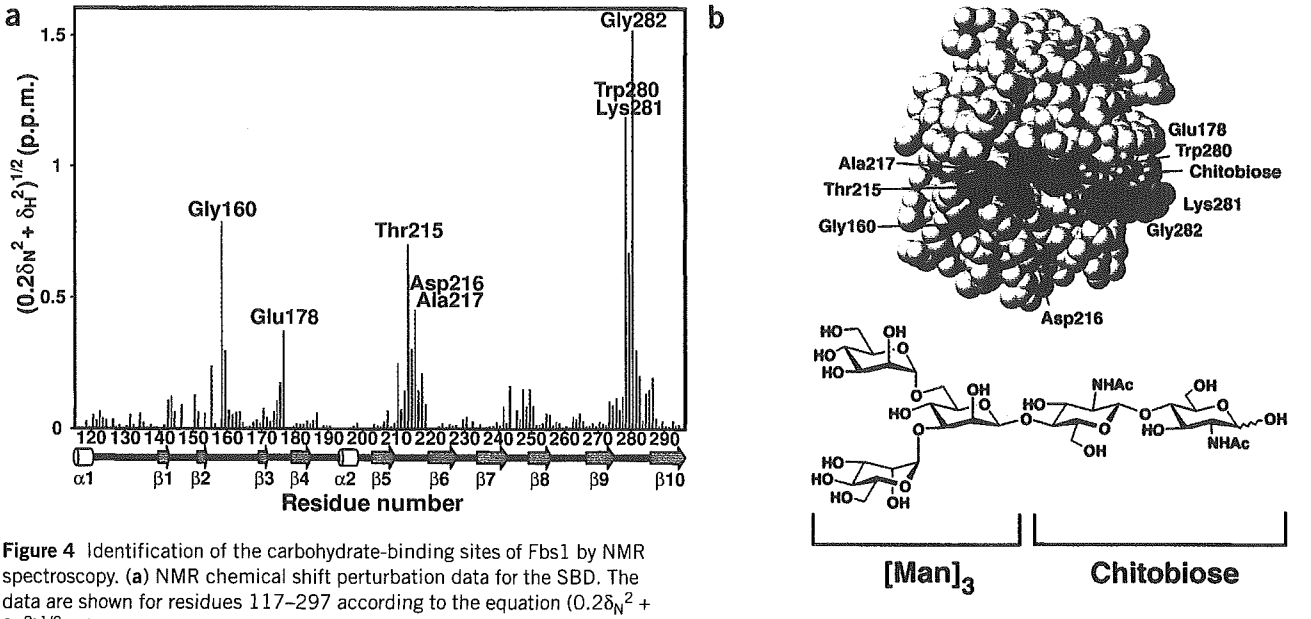


**Figure 4** Identification of the carbohydrate-binding sites of Fbs1 by NMR spectroscopy. (**a**) NMR chemical shift perturbation data for the SBD. The data are shown for residues 117–297 according to the equation $(0.2\delta_N^2 + \delta_H^2)^{1/2}$, where $\delta_N$ and $\delta_H$ represent the change in nitrogen and proton chemical shifts on addition of chitobiose (blue) and $Man_3GlcNAc_2$ (red). Secondary structure elements for SBD are shown below the plot. (**b**) Mapping the perturbed residues of the SBD(97–297) ($(0.2\delta_N^2 + \delta_H^2)^{1/2} > 0.3$) upon binding to chitobiose (blue) and $Man_3GlcNAc_2$ (blue and red). The chitobiose molecule bound to SBD is yellow. The $Man_3GlcNAc_2$ structure is represented in the right panel.

mannose branches to the interaction with Fbs1, because it is generally not feasible to crystallize or to interpret the electron density of complexes of lectins with larger oligosaccharides. To identify the oligosaccharide-binding site of the SBD in solution, we compared the pattern of the chemical shift perturbation between chitobiose and$Man_3GlcNAc_2$ (Manα1→3[Manα1→6]Manβ1→4GlcNAcβ1→4GlcNAc) using the isotopically labeled SBD (**Fig. 4** and see **Supplementary Fig. 1** online). Chitobiose binding resulted in marked chemical shift perturbation for Glu178 in the L1 loop and for Trp280, Lys281 and Gly282 in the L2 loop; this is consistent with the X-ray structure of the C132A SBD–chitobiose complex. When $Man_3GlcNAc_2$ was used as a ligand, chemical shift perturbations were observed for Gly160, Thr215, Asp216 and Ala217 in addition to the residues perturbed by chitobiose, indicating that the outer branches of the carbohydrate moiety interact with the β5–β6 loop. In the crystal structure of the SBD–chitobiose complex, O4 of GlcNAc(A) is oriented toward these amino acid residues. Thus, the orientation of the sugar chain deduced from the NMR data is consistent with the expected orientation on inspection of the crystal structure. Although mannose residues of $Man_3GlcNAc_2$ seem to interact with the β5–β6 loop of Fbs1, almost no chemical shift perturbation of any consequence was observed upon addition of mannotriose (Manα1→3[Manα1→6]Man) alone (data not shown), suggesting that the affinity of $Man_3GlcNAc_2$ is dominated by the interaction with its chitobiose portion.

## DISCUSSION

In the present study, we determined the SBD structure of Fbs1 and its complex with chitobiose. In general, most lectins bind nonreducing terminal sugar groups in the concave surface, which consists of several strands of β-sheets. The substrate-binding site of galectin-3 that forms a complex with *N*-acetyl-lactosamine is formed by β-strands[18]. The amino acids in these β-strands interact with the bound substrate through direct and water-mediated hydrogen bonds or through van der Waals contacts. In contrast, Fbs1 recognizes the inner chitobiose of N-linked high-mannose oligosaccharides by a specific binding surface located at one tip of the β-sandwich. To our knowledge, this is the first report of the sugar-binding mode of lectins, that is, interaction with the innermost portion of the carbohydrate moieties of glycoproteins. This is in marked contrast to the lectin chaperones in the ER, namely calnexin and calreticulin, which recognize nonreducing terminal glucose molecules of the high-mannose oligosaccharides expressed on their target glycoproteins.

In crystal structures of glycoproteins, electron densities of carbohydrate moieties are generally ambiguous because the carbohydrate moieties attached to the crystallized proteins do not necessarily exhibit a uniform chemical structure and may possess freedom of internal motion. In many cases, however, the innermost GlcNAc residue does provide unambiguous electron density because it is involved in interactions with the polypeptide moieties. It seems that those intramolecular interactions hamper the binding of Fbs1 to the chitobiose portions of glycoproteins as a result of steric hindrance in their native states. We propose that the novel sugar-binding mode embodied by Fbs1 is suitable for recognition of unfolded glycoproteins targeted in the ERAD system. RNase B used in the *in vitro* binding assay reveals an oligosaccharide that does not contact the polypeptide chain except at the covalent attachment point[23]. This glycoprotein could interact with Fbs1 even in the native form in the *in vitro* binding experiment, probably as a result of the exceptional freedom of the chitobiose portion of its carbohydrate moiety.

On inspection of the X-ray crystallographic and mutagenesis data, we conclude that the hydrophobic interaction between the GlcNAc(A) residue and Trp280, the hydrophobic interaction between the GlcNAc(B) residue and the small hydrophobic pocket composed of Phe177 and Tyr279, and the hydrogen bonds between the chitobiose and Fbs1 atoms, are essential for selective binding to this disaccharide moiety. Recently, we reported that Fbs2 also binds high-mannose oligosaccharides in a chitobiose-dependent manner, but the strength

**Table 1 Data collection, phasing and refinement statistics**

| **Data collection** | | | | | | | |
|---|---|---|---|---|---|---|---|
| | Native | PCMBS | $NaAuCl_4$ | $SmCl_3$ | $OsCl_3$ | $HgNO_3$ | Complex |
| Space group | $P3_221$ | | | | | | $P4_32_12$ |
| Resolution (Å) | 2.0 | 2.5 | 2.7 | 2.5 | 2.7 | 2.2 | 2.4 |
| Observations | 192,305 | 100,271 | 80,395 | 59,131 | 79,742 | 96,045 | 93,981 |
| Unique reflections | 18,483 | 9,577 | 7,689 | 9,633 | 7,695 | 13,725 | 12,611 |
| Completeness (%)[a] | 99.9 (99.9) | 99.8 (99.8) | 99.8 (99.8) | 99.8 (99.8) | 99.8 (99.8) | 98.6 (98.6) | 99.8 (99.8) |
| Redundancy[a] | 10.4 (10.1) | 10.5 (10.6) | 10.5 (10.6) | 6.1 (6.2) | 10.4 (10.5) | 7.0 (6.9) | 7.5 (7.2) |
| $R_{sym}$ (%)[a,b] | 9.5 (27.8) | 12.5 (30.6) | 9.9 (24.0) | 13.5 (22.7) | 14.3 (28.0) | 14.4 (26.4) | 8.5 (18.4) |
| $I / \sigma$[a] | 4.4 (2.5) | 4.4 (2.3) | 6.0 (2.9) | 3.9 (3.0) | 3.7 (2.3) | 3.2 (2.6) | 6.4 (3.6) |
| **MIRAS phasing** | | | | | | | |
| Resolution (Å) | 2.5 | 2.7 | 2.5 | 2.7 | 2.2 | | |
| Heavy atom sites | 3 | 2 | 2 | 1 | 2 | | |
| Phasing power | 1.37 | 0.89 | 0.76 | 1.71 | 3.31 | | |
| $R_{cullis}$[c] | 0.8 | 0.84 | 0.88 | 0.69 | 0.46 | | |
| **Refinement statistics** | | | | | | | |
| | SBD | SBD C132A–chitobiose | | | | | |
| Resolution (Å) | 2.0 | 2.4 | | | | | |
| Reflections | 17,470 | 11,950 | | | | | |
| Total atoms | 1,602 | 1,562 | | | | | |
| *R*-factor (%) | 16.2 | 20.0 | | | | | |
| $R_{free}$ (%) | 19.9 | 26.3 | | | | | |
| R.m.s. deviations | | | | | | | |
| Bond length (Å) | 0.020 | 0.038 | | | | | |
| Bond angle (°) | 1.8 | 2.9 | | | | | |

[a]Values in parentheses are for the highest-resolution shell. [b]$R_{sym} = \Sigma_h \Sigma_j |I_{hj} - \langle I_h \rangle| / \Sigma_h \Sigma_j |I_{hj}|$, where $h$ represents a unique reflection and $j$ represents symmetry-equivalent indices. $I$ is the observed intensity and $\langle I \rangle$ is the mean value of $I$. [c]$R_{cullis} = \Sigma ||F_{PH}| \pm |F_P|| - |F_H|| / \Sigma ||F_{PH}| \pm |F_P||$.

of the glycoprotein-binding ability is weaker than that of Fbs1 (ref. 8). In Fbs2, the positions corresponding to Phe177, Tyr279 and Trp280 in Fbs1 are occupied by phenylalanine, phenylalanine, and tryptophan, respectively (**Fig. 1c**). The conservation of these residues suggests that the chitobiose-binding mode of Fbs2 is similar to that of Fbs1, and the reduced binding ability of Fbs2 may be attributed to the Tyr→Phe substitution in the chitobiose-binding pocket. Fbs1 interacts not only with chitobiose at the L1 and L2 loops but also with the outer mannose residues at the β5–β6 loop. Although binding of mannose residues to the β5–β6 loop seems to strengthen the binding affinity, mannose did not bind alone. This inner chitobiose-dependent interaction mode further restricts Fbs1 to interacting with native proteins carrying high-mannose oligosaccharides. The positions corresponding to Thr215 and Ala217, which are involved in the interaction with the mannose residues, are occupied by alanine and cysteine, respectively, in Fbs2 (**Fig. 1c**). This might be associated with the distinct affinity of Fbs1 and Fbs2 to N-glycans (ref. 8).

We attempted to model the full-length Fbs1 protein and its assembly in the SCF-E2 complex by positioning the N terminus of the SBD adjacent to the F-box domain of the reported $SCF^{Skp2}$ complex[9]. This model places the chitobiose >50 Å from the expected position of the E2 protein that donates ubiquitin to the glycoprotein, consistent with modeling of other SCF complexes, such as $SCF^{Skp2}$ (ref. 9) and $SCF^{Cdc4}$ (ref. 11).

Fbs1 is a functionally unique molecule that recognizes the innermost position of N-glycans as a signal for denatured glycoproteins. Our results confirmed structurally that N-glycans act as a ubiquitination signal, thus providing new insights into the biological roles of sugar chains coupled to proteins within cells.

## METHODS

**Crystallization and structure determination.** The SBD of murine Fbs1(117–297), with a molecular mass of 20.6 kDa, and its mutant protein C132A SBD were cloned into pET15b and expressed in *Escherichia coli*. Both proteins were purified by nickel affinity and gel filtration chromatography and concentrated to 20 mg $ml^{-1}$. All mutations were constructed by QuikChange mutagenesis kit (Stratagene), using synthetic oligonucleotides, and the sequences were verified in their entirety.

Crystals of SBD were grown at 25 °C by the hanging-drop vapor diffusion method. SBD crystals were grown from 1.7 M ammonium sulfate, 0.01 M nickel chloride, 0.1% (v/v) PEG400 and 0.1 M Tris-HCl, pH 8.5. The C132A SBD was cocrystallized with chitobiose (Seikagaku). C132A SBD crystals were prepared using 1.4 M sodium chloride, 1.7 M ammonium sulfate, 0.1 M PIPES, pH 7.0, and 30 mM chitobiose. SBD and its cysteine mutant crystals belonged to $P3_221$ and $P4_32_12$ space groups, with cell dimensions of $a = b = 62.4$ Å, $c = 117.2$ Å, and $a = b = 63.8$ Å, $c = 147.8$ Å, respectively. Heavy-atom soaks were done in crystallization buffer with saturated *p*-chloromercuribenzene sulfonate (PCMBS) (for 3 h), 10 mM $NaAuCl_4$ (15 h), 10 mM $SmCl_3$ (15 h), 10 mM $OsCl_3$ (15 h) and 10 mM $HgNO_3$ (15 h). Intensity data sets were collected on a Rigaku R-AXIS IV nickel-filtered double-mirror focused CuKα-radiation detector. A Rigaku RU-200 rotating-anode X-ray generator was operated at 40 kV and 100 mA. Data were processed with MOSFLM[24] and SCALA[25,26]. The structure of the SBD was determined by the multiple isomorphous replacement anomalous scattering (MIRAS) method. Phases were calculated with MLPHARE[26] to 2.2 Å. The initial electron density map was then refined by solvent flattening[27] and histogram mapping[28] using DM[26]. The initial model was constructed with Arp/WArp[29] and O[30]. The model was refined at a resolution of 2.0 Å with REFMAC[31]. Residues 43–55 of the SBD have high temperature factors and are presumably partially disordered.

Intensity data sets of the mutant protein were collected at 100 K. For cryoprotection, 20% (v/v) glycerol was added to the crystallizing solution. The